

Reviewer #1

1. I think Part II does a rather nice job in introducing the different sources of uncertainties for SEVIRI and PROBA-V (uncertainty assessment - a necessity - is too often neglected). As a general impression though, the writing seems more of a lab “living” log, i.e. notes accumulated as the work was being carried out. You’ll notice how many of my highlighted comments aim at condensing the text as the reader might get lost in details that are often redundantly expressed. Please try and be concise. Every time you start a sentence with “In other words,”, ask yourself why you need to re-explain what you just said. As a reader, I had the impression of re-living the struggles to make sense of results, and learning a lot about the things that can go wrong while developing an algorithm, rather than walking confidently away with a message on original and reliable results. This is also reflected in grammatical hurdles. The manuscript should be proofread before submission; see countless instances of 1) “on” instead of “in”; 2) excessive use of “i.e.”, “the former” or “the latter”, “ones”, “it can be seen”, “it should be noted”, or references to other sections when not really needed; 3) missing plurals; 4) missing articles; 5) “Section” and “Figure” instead of “Sec.” and Fig.” according to the journal’s guidelines; 5) the term “miss-fit”.

The paper has been improved thanks to the detailed comments in the annotated PDF which have been implemented in this revised manuscript. Our replies are directly included in that document. Occurrences of “i.e.”, “the former”, “the latter”, ..., has been drastically reduced. The abbreviations are now in agreement with the house standards. The term miss-fit has been replaced by mismatch. The grammatical and styling suggestions have been implemented.

2. Line 116: BRF needs be defined.

TOA BRF are now spelled out separately at line 115 (now 113)

3. Section 2 concludes with “More effort would be needed to demonstrate that the forward RTM is unbiased”. This is the kind of sentences disseminated all over Part I that shake confidence in the method. This particular sentence alone gives the impression that the whole method is systematically flawed. Unless the bias is quantified being negligibly small what should the reader take away from this message? As remarked above, the draft goes at quite a length in explaining different sources of uncertainties smaller than 1%; if this last bias is larger, it would cast quite a different light on the accuracy of the method.

The accuracy of the FASTRE model has been demonstrated only against comparisons with a reference 1D RTM. We underestimated the efforts needed to demonstrate that this model can fit actual satellite data. It would require a detailed characterization of the surface and atmosphere at the overpass time which is currently lacking. It is beyond the resources we had to perform these studies and would probably require a paper of its own. We have therefore decided to remove this paragraph for the time being. We have not found in the literature similar attempts.

The assessment of FASTRE uncertainty is now described as in Part I, comparing FASTRE simulations with a reference RTM (RTMOM), and the limitations due to the 2-layer approximation are discussed. Lines 45-46, 500-501, 545-547 and 569-570 have also been removed.

- Figure 4. This way to depict the subspace of solution is misleading. For example, the way you have things set up now, the magenta triangle does not include the peak of the distribution, with $\omega > 0.98$ and $g \sim 0.75$. Lots of aerosol types are found in this region. How do you deal with this?

The aerosol vertices have been adjusted to include the peak of the distribution. Lines 206-207 of the revised paper now read “The selected CISAR vertices defining the solution space cover about the 80% of possible solutions (black triangle).”

- Fig 6. : merge the two panels into one, since you compare Carpentras with Zinder.

The merged figure looks quite confusing (Fig. 1). Even changing colors and line styles it would still not be very easy to understand. Keeping the separate panels appears a better choice.

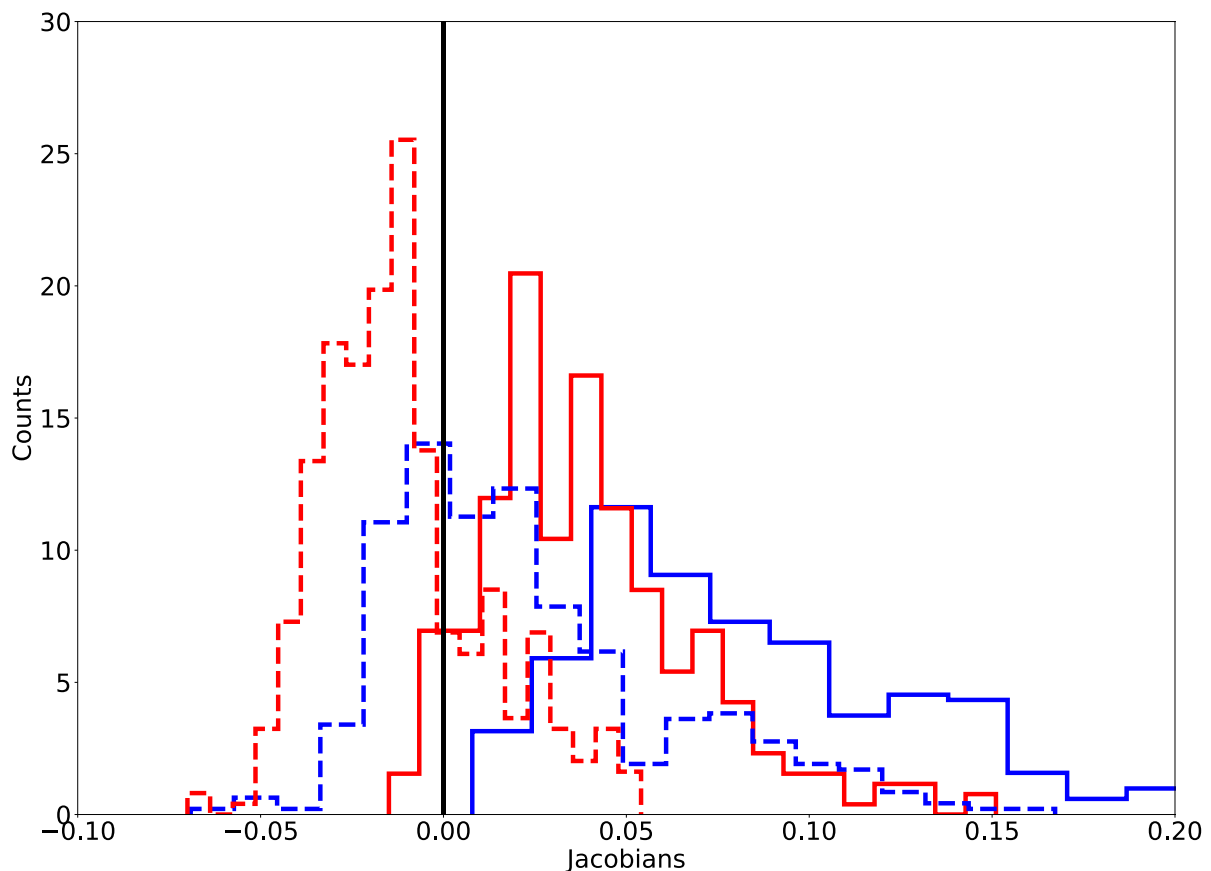


Figure 1 Merged Figure 6

- Line 280-281: this statement is simply not true and has to be reversed. While it is true that the diffraction peak is very sensitive to size, the backscattering contains tons of information (pretty much everything else). We wouldn't be doing space-based remote sensing otherwise!

Please see answer reviewer 2 regarding line 280.

- Line 283-284: what was the retrieved optical depth for this day? AND AT WHAT WAVELENGTH? This is an essential piece of information. How would the figure change if the AOT is 0.05 or 0.8? A discussion on the linearity of the AOT Jacobians is due in the text.

The retrieved optical thickness at $0.55 \mu\text{m}$ is now shown in the plot (Fig. 8) at each observation. A more detailed discussion on the AOT Jacobians magnitude can be found in Luffarelli et al. 2016 (the reference has been added in the text).

8. The “Principle” in Sec. 5.1 needs to be explained better. Please re-elaborate lines 320-330. I simply couldn’t get why the number of cloud-free pixels should be proportional to the quadratic sum of the mismatch between simulation and observation. Even in the rest of the section, I lost the logical thread. The QI/p tests part is very mysterious, I just did not get it. “QI” is not even defined, and there’s no explanation of its range of values. Please review the whole text and try to make it more understandable. Also, “miss-fit” is not a correct terminology; change to “mismatch” or something else. Little to no guidance is offered for the comprehension of Fig. 11. WHEN IS A RETRIEVAL DEEMED SUCCESSFUL?

The whole Sect. 5 has been rewritten and it is now organized as follows:

5.1 Review of existing methods

5.2 Overview

5.3 Quality indicator tests

5.4 Quality indicator computation

Section 5.3 now includes most of what was described in Sect. 5.4 which is now much shorter and, hopefully, readable. QI was defined in the introduction and according to the house standard does not have to be repeated. The term miss-fit has been replaced by mismatch. The QI/p tests part has been simplified, removing the qi definitions. Lines 346-348 (now 304-306) commenting Figure 11 (now Fig. 10) read now: “Figure 10 shows an example of the evaluation of the retrieved AOT against AERONET data for the mismatch test (3). As the mismatch increases, the correlation decreases, while the RMSE shows opposite behaviour.”

9. In both manuscripts, it’s never clear if CISAR can be applied to water and land indifferently. This should be made more clear throughout.

Line 66 (previously 69) now reads “These targets span different geometries and land cover types (vegetation, urban, bare areas, water, mixed)”. Table 1 includes both water and land cover type (it was already the case). Part I (lines 209-210) states that surface reflectance simulations over water are performed with the Cox-Munk model. However, in that case, surface reflectance is not retrieved but calculated on the basis of the surface wind considered as a model parameter.

10. The approximation of a two-layer atmosphere is not discussed. In fact, it could be a reason for the algorithm failure in many cases.

The two-layer approximation has been inherited from the approach proposed by Pinty et al. (2000) and Govaerts et al. (2010). Section 2.5 now discusses the limitations of the two-layer approximation. Lines 162-170 of the revised paper read: “The forward model uncertainty is lower than 3% in all processed bands, presenting its largest value in the SEVIRI VIS0.8 band, the most affected by water vapour absorption (Table 4). The FASTRE two-layer approximation of the atmosphere does not allow a correct discretisation of the water vapour vertical profile and, thus, a correct characterisation of its interaction with the scattering particles. Moreover, the two-layer approximation assumes that the scattering particles are only present in the lower layer. Given the spectral behaviour of the AOT, this assumption

leads to a higher uncertainty at wavelengths shorter than $0.4 \mu\text{m}$ (Seidel et al., 2010). Despite the limitations associated to the two-layer approximation, FASTRE uncertainty is in the acceptable range of 1% - 3% (Table 6).”

11. Overlap graphs in Figs. 9 and 10 so as to make one figure only

Fig. 9 and 10 are merged in one figure with 2 panels showing, for both satellites, the entropy related to the AOT and to the RPV parameters respectively.

12. Discussion following Eq. 10: it has to be made clear if you’re talking about “entropy” or “entropy difference” between pre and post retrieval.

The concept of entropy difference is never mentioned nor used in the paper. What is used is the entropy, computed as in Eq. 10 after Rodgers (2000). The entropy is mathematically defined as the logarithmic ratio between the prior uncertainty and the posterior uncertainty. It thus measures the uncertainty reduction from the prior to the posterior.

13. Sec. 5.2 is “Theoretical Concept” and comes after Sec. 5.1, i.e., “Principle”. I see no point in fragmenting the text this way. Please condense the sections.

Please see answer to comment #8

14. Line 360: it remains a mystery why a cloud mask is not applied.

“Cloud contamination” has been changed to “cloud mask omission errors”. A cloud mask is indeed applied, but omission errors might be present as discussed in Sect. 6.2 (previously 6.1).

15. Line 456-459. This is one of my most important comments. After the manuscript goes to a great length in describing a very elaborate way to aid the retrievals with “tests”, the results presented in Fig. 14 are clearly not satisfactory (a look at the correlation coefficients immediately tells that the algorithm is not retrieving appropriate AOTs). Then it is commented that at high AOTs the algorithm might fail (then why all the tests?), but that’s not too worrisome since it is better if it performs accurately at low optical depths, which are more typical. I might agree with that, but then I have to ask 1) how do you deal with the fact that the 1:1 correlation is as poor at low optical depths; and 2) why the only AOT used for testing was 0.4 in part 1.

The bias between the CISAR retrieval and the AERONET data is shown in Fig. 2, which shows different performances for SEVIRI and PROBA-V. These differences show that the bias does not only depend on the CISAR algorithm itself, but also on the quality of the processed data. The green histogram shows the AERONET AOT distribution for each bin associated with the CISAR applied SEVIRI AOT product. It can be seen there only few points correspond to $\text{AOT} > 0.8$ (less than 5% of the total number of observations), affecting the reliability of the statistics for high values of AOT. The histograms have been added in Fig. 14.

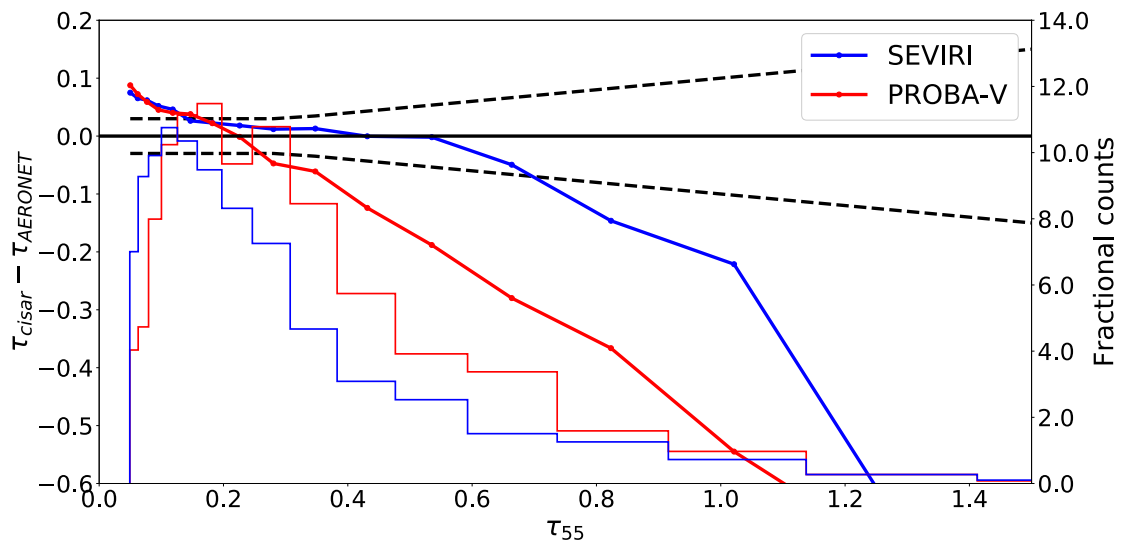


Figure 2 Bias between CISAR retrieved AOT from SEVIRI (blue) and PROBA-V (red) and AERONET data. The histograms show the distribution of the AERONET data.

The CISAR AOT product shows overestimation at low AOT and underestimation at large AOT values. The overestimation rapidly decreases as the AOT approaches values of about 0.2. The retrieval is within the GCOS requirement (dashed lines) for $0.2 < \tau < 0.75$.

For SEVIRI, two factors might explain the overestimation of the retrieved AOT below 0.2. Firstly, most of the selected AERONET stations are located in Europe as can be seen on Fig. 1 of the revised paper, where the SEVIRI pixel resolution is about 5×8 km (as opposed to 3×3 km at the subsatellite point) which is compared to AERONET point measurement. The probability of residual cloud contamination at this scale might thus explain part of the overestimation (Henderson and Chylek 2005, <https://ieeexplore.ieee.org/document/1499014/authors#authors>). Secondly (and most likely explanation), it should be reminded here that SEVIRI shortest spectral band is 0.67. At low optical thickness, e.g., 0.1, the sensitivity to aerosol at 0.67 is about 2 times smaller than in the blue spectral regions and 1.5 smaller than in the red. A preliminary analysis revealed that the sensitivity of the TOA BRF to an increase of the AOT from 0.05 to 0.15 is responsible over dark surface to a change comparable with the magnitude of the radiometric uncertainty in the 0.67 μm band. Consequently, the retrieval in these cases essentially relies on the prior information despite the very large associated uncertainty (1.0 for the fine mode, 2.0 for the coarse mode). The prior AOT magnitude is taken from the climatology proposed by Kinne et al., 2013 (doi:10.1002/jame.20035.), which exhibit typical mean values around 0.12 in the SEVIRI disk.

As concern the underestimation at large AOT, very high AOT normally correspond to local events, especially in Europe (e.g. plume, fire), therefore the AOT obtained by the retrieval from the satellite pixel containing the AERONET station will be lower than the one measured by the AERONET tower (Jiang et al., 2006, <https://doi.org/10.1016/j.rse.2006.06.022>). The processing of more data would be necessary to increase the number of points with large AOT.

Regarding PROBA-V, since the spatial resolution is one km and it has a blue band, overestimation at low AOT should not be present in the data set as is the case for SEVIRI. The retrieval from PROBA-V observations is affected by additional problems:

The poorer radiometric performances which decreases the importance of the information derived from the observations

The lack of a thermal channel that leads to an unreliable cloud mask

We acknowledge that fact that there is an issue with these results that underperform AOT retrieval with respect to other algorithms retrieving AOT from other instruments. However we are not aware of any algorithm capable of delivering a good AOT product from PROBA-V over land surfaces. Within the PV-LAC project, the CISAR benefit compared to the current operational method has been proven

(<https://earth.esa.int/web/sppa/activities/instrument-characterization-studies/pv-lac-atmo/about>).

Lines 402-409 of the revised paper read now:

“The GCOS requirements are a useful tool to compare different algorithms’ performances. However, it should be considered that both SEVIRI and PROBA-V missions were not originally designed for AOT retrieval. GCOS requirement of 0.03 for low optical thickness translates into a radiometric noise requirement much better than 2 (1)% at 0.4 (0.6) μm , i.e., way below the radiometric performance of the SEVIRI and PROBA-V instruments (Table 3). The duration of the corresponding missions provides however a decisive advantage for the generation of AOT datasets from these instruments. In the following, the GCOS requirements are evaluated in terms of percentage of retrievals satisfying them.”

Lines 410-414 of the revised paper read:

“This is in accordance with the poor radiometric performances of the polar orbiting instrument and with the outcome of the information content analysis performed in Sect. 4. The boxplots in Fig. 14 show an overestimation of the retrieval for low AOT and an underestimation for large AOT.”

Lines 412-440 of the revised paper read now:

“Additionally, very high AOT normally correspond to local events, especially in Europe e.g. plume, fire), therefore the AOT obtained by the retrieval from the satellite pixel containing the AERONET station will be lower than the one measured by the AERONET tower (Jiang et al., 2007). The histograms in Fig. 14 show that AOT values larger than 0.8 represent less than 5% of the total number AERONET observations, affecting the reliability of the statistics for high values of AOT. The processing of more data would be necessary to increase the confidence in results for high AOT values. Some examples of CISAR’s ability to detect high AOT are shown in the Supplement.

The overestimation of low AOT might originate from the different spatial scale between the satellite observations and the ground measurements. Most of the selected AERONET stations are located in Europe (Fig. 1), where the SEVIRI pixel resolution is about 5x8 km (as opposed to 3x3 km at the subsatellite point), which is compared to AERONET point measurement. The probability of residual cloud contamination at this scale might thus explain part of the overestimation (Henderson and Chylek (2005), Chand et al. (2012)). Furthermore, the shortest SEVIRI spectral band is centred at 0.67 μm , where the sensitivity to low optical thickness is about 2 times smaller than in the blue spectral region. Consequently, the retrieval in these cases essentially relies on the prior information regardless the very large associated uncertainty. Despite the presence of a blue band and a better spatial resolution (1 km), the

retrievals from PROBA-V observations still show overestimation at low AOT, due to the poorer radiometric performances which decrease the importance of the information derived from the observations and to the lack of a thermal channel that leads to an unreliable cloud mask.”

16. Line 477-480. I don't understand these comments about Fig. 17. CISAR/SEVIRI is in very good agreement? As CISAR/PROBA-V, it misses the peak of the distribution. Also, CISAR/PROBA-V is said to be underestimating the fraction but so does CISAR/SEVIRI. The significance of the ratio should also be discussed. What are typical ranges?

“Very good agreement” has been removed and replaced by “It can be seen that the distribution related to CISAR retrievals from SEVIRI and PROBA-V observations underestimate the fine mode concentration for $\tau_F/\tau_C > 3$.” I'm not sure I understand if the reviewer is referring to typical ranges of the fine/coarse mode ratio. In this case, the AERONET data can be taken as reference.

17. The relative magnitude of those “spikes” in Figs. 19 and 20 are worrisome. For the causes you attribute, shouldn't they confirm that your choice of the three vertices is inadequate?

The aerosol vertices have been adjusted as suggested by the reviewer. With the new vertices the magnitude of the spikes strongly decreases. The percentage of points falling on these values is reported in Table 1. The percentages in Table 1 are in agreement with the solution space encompassing *about* the 80% of the AERONET data.

Table 1 Percentage of SSA and Asymmetry factor retrievals falling on the spikes in Fig. 17 and 18

	w0		g	
	0.6 μ m	0.8 μ m	0.6 μ m	0.8 μ m
SEVIRI	20%	23%	8%	7%
PROBA-V	15%	31%	5%	4%

18. Line 487: I take the chance here to expand on previous comments. “Coarse mode characterization” is very far-fetched. The algorithm is not so much retrieving surface and aerosol properties, as much as two aerosol radiative properties and a set of RPV parameters while variability has not been ascertained. Even here, you've already got problems with unreliable retrievals of fine-to-coarse ratio, so much that you focus on the ratio being less or larger than 1. For these reasons, the title sounds a bit pretentious and should be adjusted accordingly. Omega and g are properties but based on the current title nowadays most readers would expect an extended set of microphysical and optical properties

Indeed, CISAR retrieves the Single Scattering Albedo and the phase function for the aerosols and the RPV parameters for the surface. As described in Part I, each of the surface parameters controls the BRF differently, describing its magnitude, shape, anisotropy and hot

spot. Any previously present reference to micro-physical aerosol properties was erroneous and has been removed. The title is therefore consistent with what the algorithm retrieves.

19. Sec. 6.3: how about Carpentras?

The timeseries is shown in Fig. 3 where the MODIS data have been filtered according to their associated quality flag

(https://lpdaac.usgs.gov/sites/default/files/public/modis/docs/MODIS_LP_BRDF+Albedo_QA_Tutorial-4.pdf). It can be seen that the MODIS timeseries shows some issues and cannot

be considered reliable. This might also partially explain the scattering in the BHR density plots in the supplements. Using MODIS to simulate satellite observations in

the attempt of proving the FASTRE capability of correctly characterise the satellite observations we underestimated the effort to collect ground truth RPV parameters.

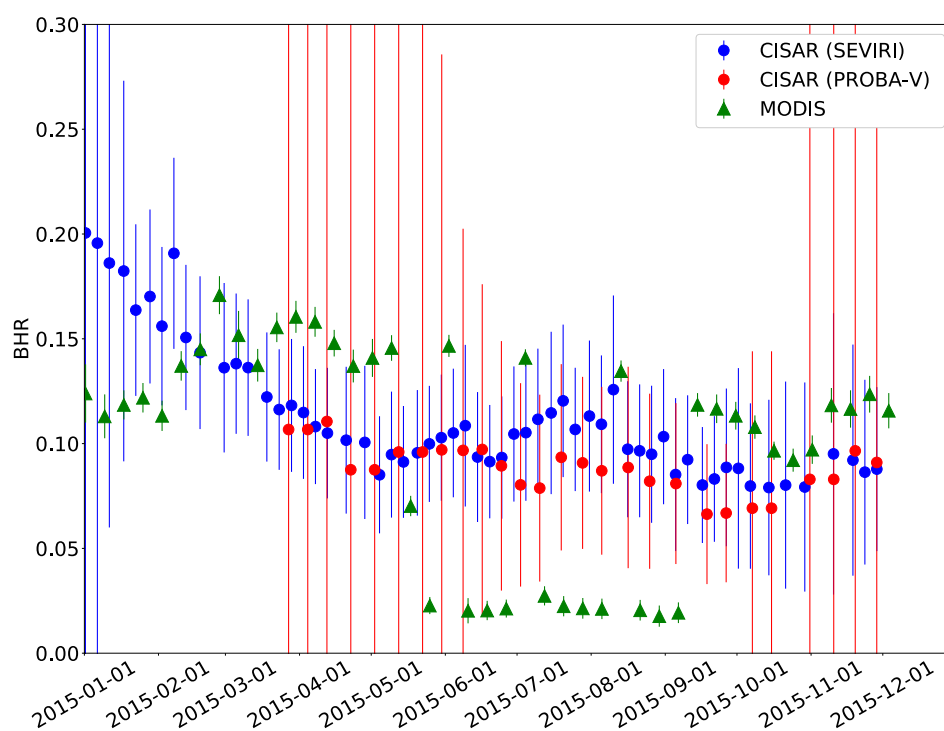


Figure 3 BHR timeseries at 0.6um over Carpentras

20. Line 545-547: This is either too obvious or a concept I don't get. You don't describe state variables, you retrieve them, so isn't just that the algorithm fails?

Following comment 3, this sentence has been removed.

21. The manuscript should report complete statistics on the number of analyzed scenes, so that the retrievals can be put in context. I'm not sure this is what happens in Table 11.

The concept of "report complete statistics on the number of analyzed scenes" is not clear. Unfortunately, we cannot answer this comment.

Reviewer #2

1. My issue is that I see no evidence that this algorithm currently produces acceptable results. Fig. 14 is not good. It's not bad enough to imply your technique is without merit, but if that's the only plot you're going to provide, you will struggle to attract interest in this algorithm as your correlation, bias and RMSE are worse than most products I've encountered. At the very least, you need to find some circumstances where your retrieval's ability to mix aerosol types produces a better retrieval than a more developed product (e.g. MODIS collection 6.1 or the Swansea University product from Aerosol CCI). Maybe biomass burning emissions from Africa or the industrial regions of China?

Please refer to the reply to Reviewer #1 for Fig. 14.

2. Also, the heritage of the algorithm and the plots in the supplement imply this method is a much better retrieval of the surface than of aerosol. I would warm to the paper more if it was arguing that you made a slightly better aerosol retrieval without harming the surface product rather than the current structure, which implies you were trying to make an aerosol retrieval and skims over the significant limitations in your current results.

Results on the surface BHR are now shown in Section 6.1 to present them prior the AOT. The following lines (506-511) are added to the discussion "The CISAR surface albedo is compared with the MODIS product, showing a correlation higher than 0.74 in all processed bands (to the exception of the NIR PROBA-V band). The better performances of CISAR in retrieving the surface reflectance rather than the AOT are explained by the larger contribution to the TOA BRF at the satellite of the surface. The little variance of the surface reflectance on a short time scale allows a good prior definition based on the previous CISAR retrievals."

3. §4 Though I'm pleased to see a discussion of information content in an atmospheric science paper, yours is rather unusual. You're using the magnitude of the Jacobian to argue which terms are the most important. However, the Jacobian has units and so the magnitude of different terms isn't direct comparable. To illustrate, consider Fig. 5, which you use to argue that ρ_0 is a more dominant driver of changes in TOA radiance than θ . A small change in surface reflectance could be of order 10^{-3} , which would produce a change of about 10^{-3} in y (as the Jacobian is approximately unity). A small change in viewing angle could be 1° and, if the Jacobian shown was in units of degrees, that would imply a change of -0.2 in y , which is much larger than that for ρ_0 . (The change is still larger if the units are radians.) The value of the Jacobian must be scaled by an appropriately small change to be compared to other values. Optimal estimation already has a mechanism to evaluate this. It's called the averaging kernel and Eq. 2.78 of Rodgers (2000) defines it as, $A = KTS^{-1}K + S^{-1}a^{-1}KTS^{-1}K$. You likely already calculate this when determining the entropy (see Eq. 2.80). A row of the averaging kernel summarises the contributions of each state vector element to the retrieval of each other variable while the diagonal elements quantify the reliance on the prior. (Things are slightly complicated by the addition of smoothing, H , terms

to your cost function. The difference is subtle; ask Oleg Dubovik about it.) For your retrieval, I would expect the diagonal of A for p_0 to be close to one and k to be closer to zero. It would also illustrate the interdependence of the different terms. I don't know if the average reader would find such an analysis easier to understand. Averaging kernels, though very powerful, are confusing. I tend to put them in supplementary material for people that care to find. If you don't switch to averaging kernels, label your plot axes as derivatives rather than Jacobians (e.g. the x-axes on Fig. 6 is $dy/d\tau$) so readers have some chance of understanding what's being plotted. More practically, I'd say a superior test to use in §5.2.4 would be the number of degrees of freedom for noise (e.g. $n - \text{tr} A$)

Thanks for your suggestions. The analysis of the information content is now performed on the Jacobians scaled on the variability range of each variable, to account for the different units. Figure 5 now shows the scaled Jacobians, and the axes are labelled accordingly. We prefer not to switch to averaging kernels as they are confusing, as explained by the reviewer.

4. §4 More generally, I'm not sure why this section is so long. It's worthwhile to point out that the retrieval's sensitivity is a function of what is observed, but there must be a more efficient way to show that the retrieval has minimal sensitivity at some times of day/year.

It is very important to discuss the challenges associated with retrieving information from satellite observations and the difficulty to get a retrieval with constant retrieval with time as the magnitude and sign of the Jacobian can change.

5. Tab. 2 This is a substantial problem. You should be more upfront about the current limitations of your method and outline in more detail what you intend to do about them. There's nothing wrong with incremental progress. This also affects L568.

The FASTRE validation is now presented in a different way. The comparison between simulations and actual observations has been removed. Now FASTRE is only evaluated against a much more accurate radiative transfer model (RTMOM) is SEVIRI and PROBA-V bands, as introduced in Part I. Please refer to the answer to the comment #3 and #19 of Reviewer #1.

6. Fig. 4 I agree with the other reviewer in wondering why you selected vertices that exclude a significant population of observed aerosols.

The aerosol vertices have been adjusted in order to encompass a wider area and include the peak of the distribution.

7. 299 I strongly suspect that there is less information content in the polar data because you ascribed more uncertainty to it (σ_c and σ_θ), not because of anything intrinsically advantageous to the geostationary view. This affects your conclusions on L555 and L561. (My opinion is that geostationary data is superior when you need temporal resolution and polar data superior when you need global coverage.)

The reviewer is right, given the larger radiometric uncertainty, PROBA-V data carry less information than SEVIRI ones. Lines 262-264 (previously 297) now read: "The distribution of the surface and AOT entropy related to SEVIRI observations exhibits higher values compared to the one related to PROBA-V observations, given the larger radiometric uncertainty associated to the observations acquired by the polar orbiting satellite.". Lines 306-310 are eliminated. Lines 549-551 (now 491-493) have been changed to: "Though the PROBA-V instrument has one blue channel which is not present on SEVIRI, the better radiometric performances of the geostationary satellite provide more information for the retrieval of surface reflectance and aerosol properties than the polar orbiting instrument.". Line 561 (currently 501-502) reads now "These differences are explained by the different information content associated to the observations acquired by the two satellites".

8. L321 Do you mean that the magnitude of the cost increases with the number of observations because there are, well, more observations? – L297 of Part 1 addressed something similar by putting a scaling into the cost function; you could do that. – The cost function is (theoretically) a χ^2 distribution with a number of degrees of freedom equal to the number of observations. Using that model, the cost can be converted into a probability that the fit is coincidental and a threshold for retrieval quality defined in terms of that (for example, keeping only retrievals with less than a 5 % probability of being the result of chance). – Regardless, I agree that filtering by cost alone will not identify retrievals with minimal sensitivity.

Thanks for your comment. Indeed, the cost function could be converted in some form of probability and used in the quality indicator computation. However, this test would be performed on the entire accumulation period rather than on a single observation. In CISAR a different QI for each observation is computed to proceed as in test 3.

9. §5 This section is very difficult to follow and needs redrafting with help from someone unfamiliar with the method. Switching between p, q, and QI doesn't help, especially when 1 is a good value for one while 0 is a good value for the other. It would be substantially easier to follow if you provided a decision tree.

The whole section has been rewritten. The term q has been removed. The terms p_i now represent the different tests. Section 5.2 now incorporates part of Sect. 5.3, leaving the latter much simpler. Good values are associated with 1, bad values with 0. It was already the case, but probably it was not very clear. Line 204 reads "Each test p_i can assume values 305 between 0 (bad quality) and 1 (good quality)." and line 369 reads "The final QI(t_i) ranges from 0 to 1, where 0 designate a poor quality retrieval and 1 indicates a reliable solution.". Please refer also to comment #8 of reviewer #1.

10. §5.2.3 Though I understand the motivation behind this test, I should point out that $y_m - y_0 \sigma_0$ is normally distributed. As such, 31.8 % of observations would be expected to fail your test by simple chance.

The reviewer is indeed right. The choice of this test and the relative thresholds derives from the choice of being more or less conservative.

11. L360 I agree with the other reviewer that the lack of discussion of a cloud masking is surprising. PROBA-V lacks thermal channels, making it difficult, but you have no problems on SEVIRI.

“Cloud contamination” has been replaced by “cloud mask omission errors”. An external cloud mask is applied (Sect. 2.3), however some clouds might not be detected and lead to the overestimation of the AOT.

12. L425 This extra test should have been mentioned back in §5.2.5. More justification of this work around is necessary.

This extra test is now mentioned in Sect. 5.2 and the following sentences (lines 362-364) are added: “Low entropy might be due to a reliable prior information, with a low associated uncertainty. Similarly, the uncertainty reduction would be very large in case of prior information with a very large uncertainty on the state variable.”

13. L453 A factor of two is not a ‘slight’ overestimation and the fact that your retrieval was this bad eight years ago does not forgive it’s failure now.

Please see answer to comment #15 of Reviewer #1.

14. L478 That isn’t good agreement. A good agreement can be seen between the red and green lines in Fig. 18(a).

The comment on Fig. 17 (now Fig. 15) reads now (lines 443-445): “It can be seen that the distribution related to CISAR retrievals from SEVIRI and PROBA-V observations seem to underestimate the fine mode concentration for $\tau_F/\tau_C > 3$.”

15. §6.2 These comparison look good! Why not give us a version of Fig. 14 for SSA and g ? Considering they’re what you retrieve, I wouldn’t be surprised if you could estimate them better than you could AOT. Wouldn’t make me think the product was any better as most users want AOT, but they aren’t many global SSA and if you could provide one, even if it’s very uncertain, that would be something worth writing about.

The correlation is strongly depends on the amount of variability in the datasets (Goodwin et al., 2006 <https://pdfs.semanticscholar.org/b6cf/001cbab0375a96c370585462dd3c163669af.pdf>). As the variability range of the aerosol single scattering properties is very limited (about 10%), we don’t find it useful to show the same kind of plot as Fig. 14.

16. L116 There are many potential calibration methods for SEVIRI. If you’re using IMPF or GSICS, could that be mentioned explicitly? If you’re using something in-house, a citation would be appreciated.

The calibration method used within this study is the one proposed by Govaerts et al. (2013), as specified in Sect. 2.2. GSICS provides routinely correction factors from IMPF values only for the thermal channels, not for the solar ones.

17. L145 Why make this approximation? Is the calculation of the other terms computationally expensive?

Yes, the calculation of the other term is computationally expensive as it implies the calculation of additional partial derivatives.

18. Eq.6 This seems a strange choice. Why not the standard deviation or interquartile range or a constant value based on climatology?

The range in which they vary is less conservative than the standard deviation or the interquartile. We don't want to impose a too strong prior. We are not using any climatology for the surface and we do not intend to.

19. §2.4(1) What's the value of N_{min} ? Why increase the uncertainty by 5 % per day rather than any other amount?

N_{min} has been added in Table 8. The prior uncertainty is increased by the arbitrary value of 5% per day in order not to rely on a solution retrieved too far away in time from the current inversion. This value has been empirically adjusted.

20. §2.5 I'd actually prefer to see a thorough sensitivity study of bias as a function of the various parameters rather than the simple 1 - 3 % uncertainty you've added, but that can be in a third paper.

Thanks for the suggestion, we might consider this for a future study. For the time being it has been implemented in this way for efficiency purposes.

21. P12L2 In my experience, the first guess is set to reduce the number of iterations needed to reach a solution. Avoiding local minima involves checking the shape of state space around the final solution or annealing (i.e. running multiple retrievals on the same data).

Indeed, one alternative solution to avoid local minima is to run multiple retrievals on the same data. However, this is also computationally expensive. The idea behind alternated first guess is to simulate the annealing running the inversion starting from different first guess for each observation, rather than repeating N times the same inversion.

22. Eq.8 So you're using a different first guess for even and odd numbered time steps? That's peculiar and, on its own, I don't see how it avoids local minima.

The first guess of the RPV parameters is not defined to minimize the probability of falling into a local minima as for the AOT. As empirical results showed that even a slight

overestimation or underestimation of the surface can lead to larger bias in the AOT retrieval, the different first guess is set to not get stuck in a over/under-estimation situation.

23. §4 The third paragraph covers four pages. Perhaps split it up.

This has been done.

24. P17L1 As the sensitivity drops through the day, I would expect the uncertainty to increase.

The AOT retrieval uncertainty depends not only on the Jacobians, but also on the temporal and spectral smoothness constraints and the quality of the surface. However Fig. 1 shows that for high Jacobians the retrieval uncertainty decreases.

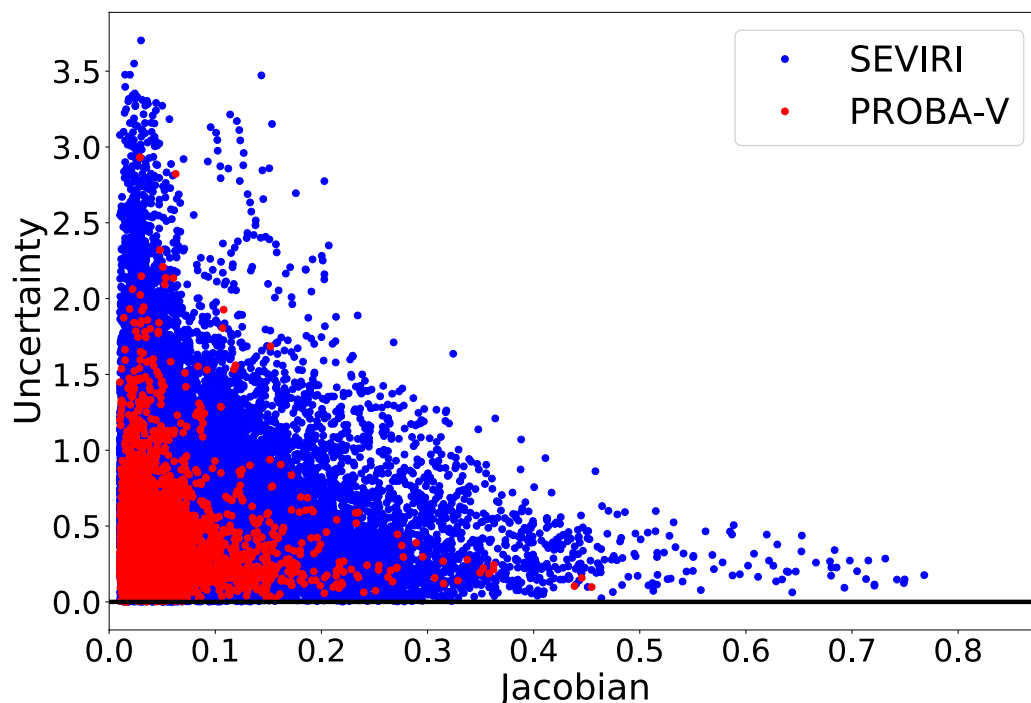


Figure 1 AOT retrieval uncertainty as a function of the Jacobians

25. L351 What is the maximum number of iterations?

It is 20, this has been added to Table 8.

26. L352 Could you clearly state that $p_0 = 1$ in all other circumstances. I wasn't certain of that till I got to Eq. 15.

This is now clearly stated. Line 352 (now 311) reads "When the maximum number of iteration is reached p_0 is equal to 0, otherwise $p_0 = 1$."

27. §5.2.2 Did you ever explore using the a priori cost for this test (i.e. the difference between the retrieval and the prior)?

Thanks for the suggestion. We might explore this option in the future.

28. Eq. 11 Aren't the y terms vectors? If so, wouldn't this require some sort of sum?

The formula is now more explicitly written:

$$\max_{\lambda} \left\{ \frac{|y_m(t_i, \lambda) - y_0(t_i, \lambda)|}{\sigma_0(t_i, \lambda)} \right\}$$

As I'm actually considering the maximum mismatch among the different bands within this test (this was not explicitly written earlier), those terms are vector components.

29. L371 Didn't you have to calculate the full Jacobian to perform your inversion? I see your point, but this is a lot of explanation for why you don't use something you should already have

I do have the full Jacobians, but considering them would require even more tests and manipulations. Anyways, as suggested from Reviewer #1, this part has been shortened

30. L379 I assume that if I ask for a justification of this statement, I will be told to go look at your papers from 2010 so I will make this sarcastic remark instead.

Indeed, in Wagner et al. (2010) the impact of the surface prior update on the covariance matrix is analysed. Furthermore, in Luffarelli et al. (2017) the effect of the updating mechanism on the retrieval is also analysed (<https://ieeexplore.ieee.org/document/8035227>).

31. Eq.15 For the sake of future readers' comprehension, please restrict q_i to the range $[0, 1]$ and make Q_i a simple product rather than use the difficult to comprehend $1 - \max(q, 1)$ construction.

The range of q_i has been restricted to $[0,1]$. However the Q_i construction cannot be replaced by a simple product as it would give the same results.

32. L409 Please specify this sigmoid function (or at least give it's width).

The width of the sigmoid function is now specified in lines 333-335 "When the mismatch assumes values within the range defined by T_1 and T_2 , thresholds excluded, a value between a minimum m and 1 is assigned to the test 3 through a sigmoid function with width equal to $10/(T_2 - T_1)$ (Fig. 11)."

33. Fig. 14 Can we please have a version of this plot as a 2D histogram in the supplement, similar to the ones already there for the BRF?

We are not sure what the reviewer refers to, as there are no histograms here for the BRF.

34. The y -axis of Figs. 5, 6, 9, 10, 15, 17, 18, 19 should probably be 'Fractional counts' considering they clearly have non-integer steps.

This has been done.

35. Fig.16 (b) and (c) aren't that interesting or helpful. Perhaps make (c) an inset in (a).

The figure has been removed.

All grammatical suggestions have been implemented.

Joint retrieval of surface reflectance and aerosol properties with continuous variation of the state variables in the solution space: Part 2: Application to geostationary and ~~polar-orbiting~~ polar-orbiting satellite observations

Marta Luffarelli¹ and Yves Govaerts¹

¹Rayference, Brussels, Belgium

Correspondence to: Marta Luffarelli (marta.luffarelli@rayference.eu)

Abstract. This paper presents the simultaneous retrieval of Aerosol Optical Thickness and surface properties ~~simultaneous retrieval~~ from the CISAR algorithm applied both to geostationary and polar orbiting satellite observations. The theoretical concepts of the CISAR algorithm have been described in Govaerts and Luffarelli (2017). ~~This paper aims to demonstrate CISAR applicability to actual~~
5 ~~satellite data acquired from different sensors flying on different orbits. For that purpose, CISAR~~
CISAR has been applied to SEVIRI and PROBA-V observations acquired over 20 AERONET stations during year 2015. The CISAR retrieval from the two instrument sets of observations is evaluated against independent datasets such as MODIS land product and AERONET data. The performance differences resulting from the two types of orbit are discussed, analysing and comparing the
10 information content of SEVIRI and PROBA-V observations.

1 Introduction

Aerosol ~~property~~ properties retrieval over land surfaces from space observation is a challenging problem due to the strong radiative coupling between atmospheric and surface radiative processes. Different approaches are usually exploited to retrieve different Earth system components (~~e.g., e.g.~~
15 Hsu et al. (2013), Mei et al. (2017)), leading to inconsistent and less accurate datasets. ~~However, data assimilation makes use of physical models, that implicitly require input data consistency.~~ The joint retrieval of surface reflectance and aerosol properties, as originally proposed by Pinty et al. (2000), presents many advantages, such as the possibility to perform the retrieval over any type of surface and assure the radiative consistency ~~between~~ among the retrieved variables.

20 Govaerts and Luffarelli (2017) (hereafter referred to as Part I) describes the theoretical aspects
of the Combined Inversion of Surface and AeRosols (CISAR) algorithm, designed for the joint
retrieval of surface reflectance and aerosol properties. This new generic retrieval method specifi-
cally addresses issues related to the continuous variation of the state variables in the solution space
within an Optimal Estimation (OE) framework. Through a set of experiments, ~~CISAR-capability-of~~
25 ~~the capability of CISAR of~~ retrieving surface reflectance and aerosol properties within the solution
space was illustrated. Nonetheless, these experiments only represent ideal simulated observation
conditions, *i.e.*, noise free data acquired in narrow spectral bands placed in the principal plane,
assuming unbiased surface prior information. This second part aims to demonstrate CISAR's ap-
plicability to actual satellite observations, with less favourable geometrical conditions than the
30 principal plane and accounting for the radiometric noise. For this purpose, the algorithm has been
applied to two radiometers with similar spectral properties but different orbits, (geostationary and
polar). Radiometers on board of geostationary platforms deliver observations with a revisit time ~~in~~
~~the range of several tenth~~ of ~~tens of~~ minutes but with a limited field of ~~regard-view~~ so that many
~~different instruments with different sub-satellite locations-instruments~~ are needed to cover the entire
35 Earth. ~~Poles-The poles~~ cannot be observed. Conversely, a polar orbit, combined with an adequate
swath, could offer a daily revisit time of the entire globe. The selected radiometers are the Spinning
Enhanced Visible and Infrared Imager (SEVIRI), flying on board of the Meteosat Second Genera-
tion (MSG) geostationary platform, and the ~~Project-Project~~ for On-Board Autonomy - Vegetation
(PROBA-V). These two instruments have ~~pretty~~ similar radiometric performances and both have
40 acquired more than 15 years of observations thanks to the launch of a succession of radiometers
with very similar characteristics. Applying the same algorithm on similar instruments ~~but flying~~
~~on flying in~~ different orbits represents a meaningful way to analyse the CISAR generic algorithm
performance ~~when applied on actual data~~.

This paper is organised as follows. Section 2 describes the observation system considered in the
45 OE framework, the satellite observation, the ancillary information, the prior information and the
forward model. The ~~capability of the latter to correctly simulate satellite observations is evaluated,~~
~~this being one of the fundamental OE method prerequisites.~~ The uncertainty characterisation of the
observation system is also described in ~~Section 2~~ Sect. 2. The algorithm implementation is described
in ~~Section~~ Sect. 3. Section 4 analyses the information content of the satellite observations, com-
50 paring the differences between the geostationary and polar orbiting instruments, and discusses the
challenges encountered when little or no information about the retrieved variables is carried by the
observation. Given these difficulties in the retrieval, a Quality Indicator (QI) is implemented and pre-
sented in ~~Section~~ Sect. 5, characterising the reliability of the solution. Finally, ~~CISAR performances~~
~~are the performance of CISAR is~~ discussed in detail in ~~Section 6~~ Sect. 6. The CISAR retrieved
55 Aerosol Optical Thickness (AOT) and Bidirectional Hemispherical Reflectance (BHR) will be com-
pared against those derived from the Aerosol Robotic Network (AERONET) (Giles et al., 2017) and

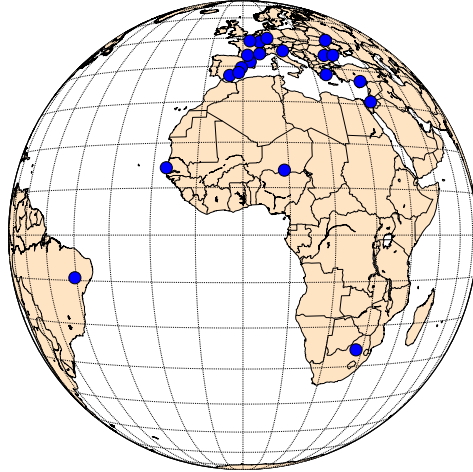


Fig. 1: Selected AERONET stations location. All stations are located within the SEVIRI field of regard view.

the Moderate Resolution Imaging Spectroradiometer (MODIS) Land product data (DAAC, 2017), respectively. The performance differences between the ~~two retrieved datasets~~ retrieved datasets obtained from SEVIRI and PROBA-V observations will be further investigated through statistics on the quality of the retrieval and through the information content of the satellite observations.

2 ~~Observations~~ Observation system characterisation

2.1 ~~Definition~~ Observation system definition

The fundamental principle of the OE is to maximise the probability $P = P(\mathbf{x} | \mathbf{y}_{\Omega\tilde{\Lambda}}, \mathbf{x}_b, \mathbf{b})$ with respect to the values of the state vector \mathbf{x} , conditional to the value of the measurements and any prior information (Rodgers, 2000). The ensemble of measurements, prior information, ancillary data and the forward model constitutes the observation system. This ~~Section~~ section describes each component of this system for the two satellite datasets processed in the framework of this study.

In order to evaluate the CISAR algorithm ~~'s performances when applied on observations acquired with performance when applied to observations acquired from~~ different orbits, 20 AERONET stations located within the SEVIRI field of ~~regard view~~ regard view have been selected (Fig. 1, Table 1) ~~and the corresponding observations were acquired for year 2015. These targets have been selected in order to have.~~ These targets span different geometries and ~~different~~ land cover types (vegetation, urban, bare areas, ~~mixed~~), ~~based on the availability of AERONET observations.~~ water, mixed. The observations pertain year 2015.

Table 1: AERONET targets

Name	Latitude	Longitude	Land Cover Type
Athens_NOA	37.99	23.77	Urban
Barcelona	41.39	2.12	Urban
Bucharest_Inoe	44.35	26.03	Mixed
Bure_OPE	48.56	5.50	Vegetation
Burjassot	39.51	-0.42	Urban
Carpentras	44.08	5.06	Vegetation
Dakar	14.39	-16.96	Costal
Gloria	44.60	29.36	Water
Granada	37.16	-3.60	Urban
IMS-METU-ERDERMLI	36.56	34.25	Costal
Kyiv	50.36	30.50	Vegetation
Mainz	49.50	8.30	Mixed
Murcia	38.01	-1.17	Vegetation
Paris	48.87	2.33	Urban
Petrolina_SONDA	-9.38	-40.50	Urban
Pretoria_CSIR-DPSS	-25.76	28.28	Mixed
Sede_Boker	30.85	34.78	Bare Areas
Toulouse_MF	43.57	1.37	Urban
Venise	45.31	12.51	Water
Zinder_Airport	13.78	8.99	Bare Areas

75 For each of these stations, satellite data have been acquired, together with ancillary information, such as the cloud mask and the model parameters, ~~which are~~ all the parameters that are not retrieved by the algorithm but ~~that~~ influence the observation. Satellite data and ancillary information are accumulated in time to form a multi-angular observation vector $\mathbf{y}_{\Omega\tilde{\lambda}}$, in order to correctly characterise the surface ~~anisotropy reflectance anisotropy~~. Nevertheless, retrieving surface and aerosol properties
80 from satellite observations is an ill posed problem (~~Hadamard, 1902~~)(Wang, 2012). Consequently, assumptions on the magnitude and ~~on the~~ temporal/spectral variability of the state variables are made. The ensemble of these assumptions and their associated uncertainties constitutes the prior information.

The observation uncertainty σ_o characterisation is one of the most critical aspect of ~~the~~ CISAR
85 algorithm as it ~~strongly directly~~ determines the likelihood of the solution. In fact~~the observation uncertainty~~, ~~σ_o~~ determines the observation term ~~value~~ of the cost function ~~as in~~ (Eq. 17 ~~in Part I,~~ thus impacting the minimization process. ~~σ_o is composed by of Part I). The observation uncertainty is composed of~~ the radiometric uncertainty, directly related to the radiometer characteristics, the forward model uncertainty ~~in the observed bands~~ and the uncertainty related to the model parameters.

90 2.2 Satellite data

MSG nominal position is 0° over the equator in a geostationary orbit. SEVIRI is the main instrument of the MSG mission, which has as primary objective the observation in the near real-time of the Earth's full disk, shown in Fig. 1. SEVIRI achieves this with 12 channels, ranging from 0.6 μm to 13 μm , three of which are located in the solar spectrum and centred at 0.64 μm , 0.81 μm and ~~1.64 μm~~ 1.64 μm and are used within this study. SEVIRI observes the Earth's full disk with a 15 ~~minutes~~ minute repeat cycle. ~~MSG nominal position is 0° over the equator in a geostationary orbit.~~ The sampling distance between two adjacent pixels at the sub-satellite point is 3 km for the visible bands. As there is no on-board device for the calibration of the solar channels, ~~their calibration~~ the calibration within this study has been performed with the method proposed by Govaerts et al. (2013).

100 PROBA-V satellite mission is intended to ensure the continuation of the Satellite Pour l'Observation de la Terre 5 (SPOT5) VEGETATION products since May 2014 (Sterckx et al., 2014). The microsatellite offers global coverage of land surface with daily revisit for latitude from 75°N to 56°S in four spectral bands, centred at 0.46 μm , 0.66 μm , 0.83 μm and 1.61 μm . The PROBA-V products are provided at a spatial resolution of 1/3 km and 1 km, the latter being used ~~within in the~~ framework of this study. To cover the wide angular field of view (101°) in a small-sized platform, the optical design of PROBA-V is made up of three cameras (identical three-mirror anastigmatic (~~TMA~~) telescopes). The three cameras have an equal field of view, ~~the central camera pointing down.~~ The down-pointing central camera covers a swath ~~of~~ 500 km wide, while the swath of the right and left cameras ~~cover is~~ 875 km each wide. Although the three cameras have different responses, a mean 110 Spectral Response Functions (SRF) is considered within this study, accounting for the radiometric uncertainty associated with this approximation. Each camera has two focal planes, one for the short wave infrared (SWIR) band and one for the visible and near-infrared (VNIR) bands. Despite the different viewing angles in the SWIR band, CISAR assumes the observations are acquired with the same geometry in all bands. This assumption leads to an additional term in the observation uncer- 115 tainty. Because of the omission of on-board calibration devices, the PROBA-V in-flight calibration relies only on vicarious methods (Sterckx et al., 2013).

The similarities between the three SEVIRI solar bands and the red, NIR and SWIR ~~PROBA-V~~ PROBA-V bands permit the evaluation and comparison of the CISAR performances when applied to the two instruments, ~~which whose~~ spectral responses are shown in Fig. 2. The satellite obser- 120 vations have been acquired from the European Organisation for the Exploitation of Meteorological Satellites (~~EUMETSAT~~ EUMETSAT) Earth Observation Portal and from the Flemish Institute for Technological Research (VITO) for SEVIRI and PROBA-V respectively. The Top Of Atmosphere (~~TOA~~) Bidirectional Reflectance Factor (~~TOA~~-BRF) is computed directly from the digital count value in case of SEVIRI, ~~whereas whereas~~ for PROBA-V the Level 2-A TOA BRF is ~~delivered~~ 125 provided by VITO (Wolters et al., 2018). The satellite observation uncertainty is derived from the radiometric noise σ_i ~~and~~ the geolocation uncertainty σ_r . For PROBA-V two additional terms are calculated: the uncertainty σ_c associated to the approximation of a mean SRF of the cameras and

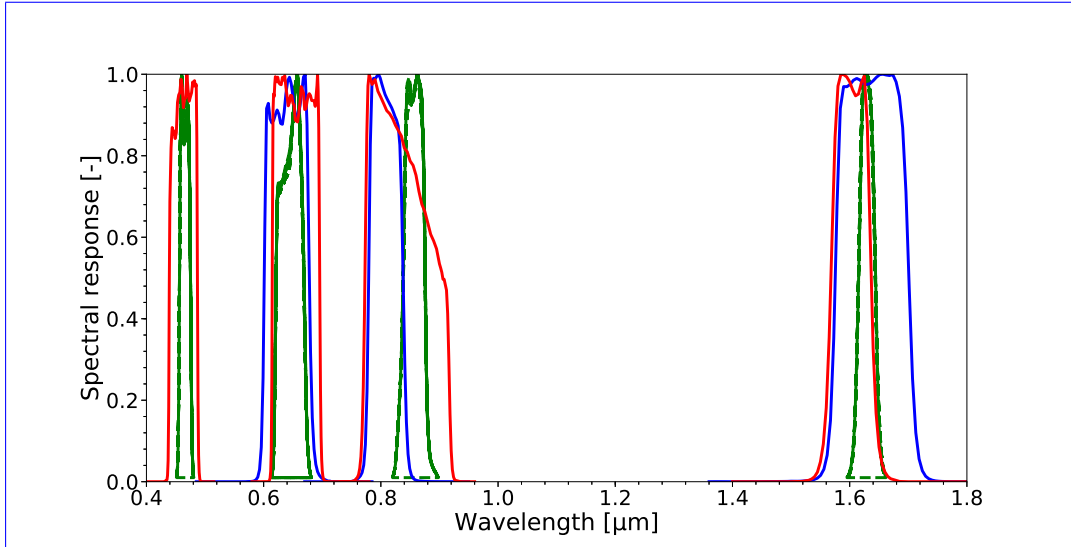


Fig. 2: SEVIRI (in blue), PROBA-V (in ~~green~~red) and MODIS (in ~~magenta~~green) spectral responses.

Table 2: PROBA-V instrument noise [%]

Band	Left camera	Center Camera	Right Camera
BLUE	4	4	4
RED	3	3	3
NIR	3	3	3
SWIR	5	4	5

the one deriving from considering the same viewing geometry in the SWIR and in the VNIR bands,

$\sigma_{\theta}\sigma_{\Omega}$.

PROBA-V radiometric noise has been delivered by VITO (Sindy Sterckx, personal communication, September 2017) per camera and per band [Table 2 \(Table 2\)](#). For SEVIRI, this term is computed considering (i) the instrument noise due to the dark current, (ii) the difference between the detectors gain and (iii) the number of digitalization levels (Govaerts and Lattanzio, 2007). The geolocation uncertainty σ_r , arising from the assumption of ~~observing always the same scene~~[the satellite data being correctly mapped to the surface of the Earth](#), is estimated for each pixel \mathbf{p} as follows (Govaerts et al., 2010):

$$\sigma_r^2(t, \tilde{\lambda}, \mathbf{p}) = \left(\frac{\partial \mathbf{y}_0(t, \tilde{\lambda}, p_x, p_y)}{\partial p_x} \sigma_x(t, \tilde{\lambda}) \right)^2 + \left(\frac{\partial \mathbf{y}_0(t, \tilde{\lambda}, p_x, p_y)}{\partial p_y} \sigma_y(t, \tilde{\lambda}) \right)^2 \quad (1)$$

130 where $\sigma_{x,y}$ is the geolocation/coregistration standard deviation and $\mathbf{y}_0(t, \tilde{\lambda}, p_x, p_y)$ is the TOA BRDF in the channel $\tilde{\lambda}$ acquired at the time t .

The uncertainty σ_c , originating from the usage of a mean SRF for the three ~~PROVA-V~~[PROBA-V](#)

cameras, has been estimated simulating the TOA BR_F considering both the mean and actual SRF for a wide range of observation conditions. The assessed σ_c ~~results is~~ lower than 0.2% in all bands and for all cameras. Finally, the assumption of having the same viewing geometry for the three PROBA-V bands is associated to the uncertainty $\sigma_{\theta}\sigma_{\Omega}$, computed as follows:

$$\sigma_{\Omega}^2(t, \tilde{\lambda}, \Omega, \mathbf{p}) = \left(\frac{\partial \mathbf{y}_0(t, \tilde{\lambda}, \theta)}{\partial \theta} \sigma_{\theta}^2(t, \tilde{\lambda}) \right) \quad (2)$$

The total relative radiometric uncertainty median values are shown in Table 3.

2.3 Ancillary data

In addition to satellite observations, a cloud mask and the model parameters information are required. For SEVIRI observations, the nowcasting Satellite Application Facility (SAF) cloud mask (Meteo France, 2013), provided at the radiometer's native temporal and spatial resolution, is used; for PROBA-V the cloud mask is provided by VITO (Wolters et al., 2018). The model parameters, *i.e.*, Total Column Water ~~Vapor~~ Vapour (TCWV), Total Column Ozone (TCO₃) and surface pressure are taken from the European Centre for Medium-Range Weather Forecasts (ECMWF) reanalysis (Dee et al., 2011).

The uncertainties of the **equivalent** model parameters \mathbf{b} are converted into an equivalent noise σ_B , calculated as follow (Govaerts et al., 2010):

$$\sigma_{FB}^2(\mathbf{b}, \tilde{\lambda}, \Omega_0, \Omega_v) = \left(\frac{\partial y(\mathbf{x}, U_{oz}; \Omega, \tilde{\lambda})}{\partial U_{oz}} \sigma_{U_{oz}} \right)^2 + \left(\frac{\partial y(\mathbf{x}, U_{wv}; \Omega, \tilde{\lambda})}{\partial U_{wv}} \sigma_{U_{wv}} \right)^2 + \left(\frac{\partial y(\mathbf{x}, U_{sp}; \Omega, \tilde{\lambda})}{\partial U_{sp}} \sigma_{U_{sp}} \right)^2 \quad (3)$$

where U_{oz} , U_{wv} are the ozone and water vapour total column concentration ~~and~~, U_{sp} is the surface pressure and $\sigma_{U_{oz}}$, $\sigma_{U_{wv}}$ and $\sigma_{U_{sp}}$ are their associated uncertainties. The surface pressure contribution to the signal is about 10 times smaller than the contribution of the water vapour concentration. The TCWV is distributed among the two atmospheric layers in the forward radiative transfer model assuming a US76 water vapour vertical profile (Sissenwine et al., 1976). The fraction of TCWV in the scattering layer interacts with the aerosol particles and thus strongly ~~affect~~ affects the CISAR retrieval. Unlike the ozone which is mainly present in the stratosphere, the water vapour is dominant in the lower part of the atmosphere, severely impacting the aerosol retrieval in SEVIRI and PROBA-V band 0.8 μm (Table 4). Hence, only the uncertainty related to the TCWV is

Table 3: Total radiometric uncertainty median values [%]

	0.4 μm	0.6 μm	0.8 μm	1.6 μm
SEVIRI		<u>2.73</u> <u>3</u>	<u>2.24</u> <u>2</u>	<u>3.12</u> <u>3</u>
PROBA-V	<u>4.01</u> <u>4</u>	<u>3.04</u> <u>3</u>	<u>3.02</u> <u>3</u>	<u>4.03</u> <u>4</u>

155 considered and Eq. 3 is approximated to:

$$\sigma_{FB}^2(\mathbf{b}, \tilde{\lambda}, \Omega_0, \Omega_v) \approx \left(\frac{\partial y(\mathbf{x}, U_{wv}; \Omega, \tilde{\lambda})}{\partial U_{wv}} \sigma_{U_{wv}} \right)^2 \quad (4)$$

The median values of the Equivalent Model Parameter Noise (EQMPN), computed as in Eq. 4, are shown in Table 5.

2.4 Prior information

160 Within an OE framework, the definition of the prior information and its uncertainty plays a fundamental role. In CISAR four different sources of prior information are considered:

1. Surface parameters magnitude. The surface reflectance, represented by the RPV (Rahman-Pinty-Verstraete) model (Rahman et al., 1993), is not ~~supposed-expected~~ to undergo rapid ~~variation-variations~~ on a short temporal scale, hence the retrieval in the previous accumulation period can be used as prior information for the next inversion (Govaerts et al., 2010). ~~Therefore~~ ~~the-The~~ prior information on the RPV parameters at the time t_d is built computing a running mean over the N_r ~~previous-successful~~ ~~previously-converged~~ accumulation periods.

$$\mathbf{x}_b(t_d) = \frac{\sum_{t_i=0}^{t_d-1} \hat{\mathbf{x}}(t_i)}{N_r} \quad (5)$$

The corresponding prior uncertainty is defined as half of ~~the~~ variability range of the solution $\hat{\mathbf{x}}(t_i)$ retrieved during the considered N_r accumulation periods.

$$\sigma_{\mathbf{x}_b}(t_d) = \frac{\max_{t \in N_r} \hat{\mathbf{x}}(t_i) - \min_{t \in N_r} \hat{\mathbf{x}}(t_i)}{2} \quad (6)$$

When N_r is smaller than a certain minimum ~~required-threshold~~ N_{min} (Table 8), the prior information on the magnitude of the RPV parameters is taken from the last successful retrieval and its uncertainty is computed as in Eq. 7, where N_d is the number of days since the last successful retrieval (Govaerts et al., 2017).

$$\sigma_{\mathbf{x}_b}(t_d) = \sigma_{\mathbf{x}_b}(t_d - 1) 1.05^{N_d} \quad (7)$$

Table 4: Water Vapour transmittance in the SEVIRI, PROBA-V and MODIS bands

	0.4 μm	0.6 μm	0.8 μm	1.6 μm
SEVIRI		0.993	0.915	0.988
PROBA-V	1.000	0.990	0.926	0.995
MODIS	1.000	0.990	0.985	0.996

Table 5: Total EQMPN median values [%]

	0.4 μm	0.6 μm	0.8 μm	1.6 μm
SEVIRI		0.28	2.02	0.38
PROBA-V	0.01	0.37	1.49	0.14

2. AOT magnitude: ~~this~~. This information is taken from an annual mean climatology dataset (Kinne et al., 2013). From this dataset, the prior information on the AOT magnitude for the coarse and fine mode (absorbing and non absorbing distinctly) is taken. The uncertainty is set to a high arbitrary value σ_{x_b} for all the wavelengths (Table 8).
- 165 3. Constraints on the AOT temporal variability. These constraints result from the assumption that the AOT is not changing rapidly on a very short temporal scale, therefore a maximum temporal variation is defined through a ~~sigmoide~~ sigmoid function. The temporal constraints are described by the matrix \mathbf{H}_a in Eq. 13 of Part I.
- 170 4. Constraints on the AOT spectral variability. The AOT is expected to decrease with the wavelength, ~~according to~~ proportionally to the ratio of the extinction coefficient (see Eq. 15 of Part I). The applied constraints define the matrix \mathbf{H}_l ~~as in~~ (Eq. 14 of Part I).

2.5 Forward model

FASTRE, the CISAR forward Radiative Transfer Model (RTM), and its uncertainty σ_F are described in ~~Section Sect.~~ 4.4 of Part I. ~~The forward model uncertainty has been estimated for FASTRE uncertainty in the~~ SEVIRI and PROBA-V processed bands ~~(Table 6). The OE method relies on the assumption that the forward model used in the inversion process is capable of correctly representing the observation. The verification of this assumption is important but difficult to realise in practice. To evaluate the validity of this assumption, a simulated dataset has been prepared with FASTRE and compared with the actual observations acquired by the two satellites in 2015 over the selected stations. To simulate the satellite observations, FASTRE requires to know the value of the state variable (RPV parameters, AOT) and model parameters (TCWV, TCO₃, Surface Pressure). The latter are taken from ECMWF reanalysis. The RPV parameters are derived from the MODIS Land Product MCD43A Collection 5 (Schaaf and Wang, 2015). The MODIS product delivers the RossLi parameters (Li and Strahler (1992), Ross (1981), Wanner et al. (1995)), from which the surface BRDF can be computed. The RPV model has been inverted against this calculated BRDF field to retrieve the corresponding RPV parameters. The AOT is derived from AERONET V3 L2.0 (Giles et al., 2017) , present only in clear sky conditions. The results of this evaluation are shown in Table 7. The correlation between the simulated data and actual observations exceed 0.9 in all spectral bands with a Root Mean Square Error (RMSE) that does not exceed 0.06. The relative bias exhibits values that~~

175

180

185

190 ~~can exceed~~ has been estimated as in Eq. 10 %. ~~Several factors can explain these large values.~~ of Part I, comparing the outcome of FASTRE with a more elaborated RTM, where 50 atmospheric layers are considered. The results of this evaluation are shown in Table 6. The forward model uncertainty is lower than 3% in all processed bands, presenting its largest value in the SEVIRI VIS0.8 band, the most affected by water vapour absorption (Table 4). The FASTRE two-layer approximation of
 195 the atmosphere does not allow a correct discretisation of the water vapour vertical profile and, thus, a correct characterisation of its interaction with the scattering particles. Moreover, the two-layer approximation assumes that the scattering particles are only present in the lower layer. Given the spectral behaviour of the AOT, this assumption leads to a higher uncertainty at wavelengths shorter than 0.4 μm (Seidel et al., 2010). Despite the limitations associated to the two-layer approximation,
 200 FASTRE uncertainty is in the range of 1% - 3% (Table 6), which is smaller or equal to the instrument radiometric noise.

The spectral responses of SEVIRI, PROBA-V and MODIS are shown in Fig. 2. The different band widths and center wavelengths result in differences in the gaseous absorption, as shown in Table 4. The latter is particularly important for the water vapour, as it interacts with the aerosol particles in
 205 the FASTRE scattering layer. As it can be seen from Table 4, the water vapour absorbance strongly affects the bands centred around 0.8 μm , thus impacting the signal acquired by the three different radiometers. The different spectral responses of the three instruments, and the associated gaseous absorption, represents thus a limitation to the FASTRE model evaluation against actual observation. Furthermore, although the MODIS product provides a measure of the surface reflectance, its true
 210 value remains unknown. The lack of accurate characterisation of the surface BRDF in the SEVIRI and PROBA-V spectral bands represents also a limitation to this first FASTRE model direct comparison against actual observations. This specific point would require additional effort with dedicated ground observations. The AOT observed by the satellites could also differ from the AERONET one, given the larger spatial resolution of the satellite observations, which could results in cirrus contamination
 215 or neighbouring aerosol events not caught by the AERONET measure. Given these considerations, although FASTRE simulated satellite observations with a correlation of about 0.9 and in a first approximation results suitable for inversion purposes, more effort would be needed to demonstrate that the forward RTM is unbiased.

Table 6: FASTRE relative uncertainty in the SEVIRI and PROBA-V processed bands [%]

	0.4 μm	0.6 μm	0.8 μm	1.6 μm
SEVIRI		1.88	2.75	0.96
PROBA-V	2.38	1.31	2.20	0.75

Table 7: Comparison between FASTRE simulations and the actual SEVIRI and PROBA-V TOA BRF observations

	SEVIRI			PROBA-V			
	VIS0.6	VIS0.8	NIR1.6	BLUE	RED	NIR	SWIR
Correlation	0.96	0.93	0.95	0.91	0.98	0.96	0.98
Root Mean Square Error	0.03	0.06	0.06	0.02	0.03	0.04	0.03
Relative Bias %	11.02	17.66	8.55	6.42	16.65	8.54	6.01

3 Data processing

220 3.1 General setup

The theoretical concepts of the CISAR algorithm have been described in Part 1. In order to perform the inversion on actual satellite data, the observations are accumulated in time and the corresponding uncertainty is computed as described in Section Sect. 2. This temporal accumulation is performed in order to build a multi-angular observation vector $\mathbf{y}_{\Omega\lambda}$ to characterise ~~surface~~ the surface reflectance anisotropy. The surface optical properties are considered invariant during the accumulation period, ~~hence and therefore~~ a trade-off between having enough cloud free observations to build the observation vector and allowing the algorithm to catch surface variations is introduced; the ~~high repeat~~ high-repeat temporal coverage of geostationary satellites allows a shorter accumulation periods with respect to polar orbiting instruments. For SEVIRI acquisitions, although the angular sampling does not vary much from one day to the next, the length of the accumulation period is set to 5 days in order to maximise the occurrence of cloud free observations. For polar orbiting satellite satellites, the length of the temporal accumulation is normally driven by the repeat cycle, as it is ~~done for MODIS observations the case for MODIS~~ (DAAC, 2018). In the case of PROBA-V, the satellite orbit is not maintained ~~;~~ and there is no repeat cycle. Hence, the choice of the length of the time window during which the satellite observations are accumulated results from empirical studies ~~aim to balance~~ aims at balancing the trade-off previously described. Consequently, the length of the accumulation is set to 16 days and the successive accumulation periods are shifted by 8 days. An example of the angular sampling during this accumulation period is shown in Fig. 3 for SEVIRI and PROBA-V. During the accumulation process period, observations acquired with a sun ~~and or~~ viewing angle larger than θ_{max} (defined in Table 8) are discarded. CISAR setup parameters

~~N_a Length of the accumulation period 5-16 N_s Shift between the accumulation period 5-8 θ_{max} Maximum processed sun and viewing zenith angles $^\circ$ 70-70 τ_{low} Minimum AOT first guess value 0.001-0.001 τ_{high} Maximum AOT first guess value 0.100-0.100 $\sigma_{x_b,TF}$ Fine mode prior uncertainty for the AOT 1.0-1.0 σ_{x_b,τ_C} Coarse mode prior uncertainty for the AOT 2.0-2.0 $\sigma_{x_b,RPV}$ Default prior uncertainty for the RPV parameters 1.0-1.0~~

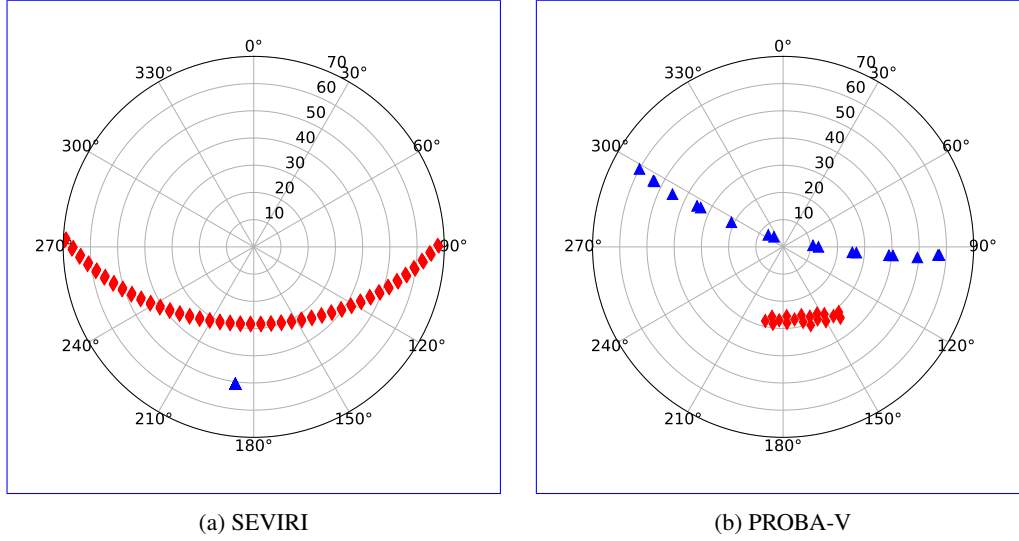


Fig. 3: Polar plot of the angular sampling during a 5 days (2015/05/01-2015/05/05) of SEVIRI observations (left panel) and during 16 days (2015/05/01-2015/05/16) of PROBA-V observations (right panel) over Carpentras, France. The blue triangles represent the [satellite viewing geometry angles](#), the ~~yellow-red~~ diamonds the illumination one. Circles represent the zenith angle and polar angles represent azimuth angles with zero azimuth pointing to the North.

~~At the end of this accumulation period the inversion takes place.~~ The definition of the first guess is an important aspect of the inversion process and it is defined in order to minimise the possibility of finding local minima. When a minimum value is found, an [exploration investigation of the cost function in the vicinity of the solution](#) should be made in order to determine whether or not it is a local minimum. However, this exploration could be computationally expensive. In order to minimise the possibility of local minima without degrading the computational performances, the AOT first guess is [set assigned to successive observations](#) alternating between a low value τ_{low} and a larger one τ_{high} (see Table 8). As CISAR retrieves one single set of RPV parameters over the entire [accumulation](#) period in each processed band, only one set of first guesses \mathbf{x}_0 is defined:

$$\mathbf{x}_0(t_d) = \mathbf{x}_b(t_d) + (-1)^{i_{t_d}} * \sigma_{\mathbf{x}_b}(t_d) \quad (8)$$

where i_{t_d} is the index of the current accumulation period and \mathbf{x}_b is the prior information at the accumulation period t_d .

From the retrieved set of RPV parameters the BHR is calculated, assuming perfectly diffuse illumination conditions, and the AOT is extrapolated at $0.55 \mu\text{m}$ through the extinction coefficient α :

$$\tau_{0.55,v} = \tau_{\lambda,v} \left(\frac{\alpha_{0.55,v}}{\alpha_{\lambda,v}} \right) \quad (9)$$

where v is the considered aerosol vertex and λ is the wavelength from which the AOT at $0.55 \mu\text{m}$ is extrapolated. ~~The setup parameters are summarized in Table 8.~~

Table 8: CISAR setup parameters

		SEVIRI	PROBA-V
N_d	<u>Length of the accumulation period</u>	<u>5</u>	<u>16</u>
N_s	<u>Shift between the accumulation period</u>	<u>5</u>	<u>8</u>
N_{min}	<u>Minimum converged retrievals to compute the mean on the RPV parameters</u>	5	5
\sim	<u>Maximum number of iterations</u>	<u>20</u>	<u>20</u>
θ_{max}	<u>Maximum processed sun and viewing zenith angles [°]</u>	<u>70</u>	<u>70</u>
τ_{low}	<u>Minimum AOT first guess value</u>	<u>0,001</u>	<u>0,001</u>
τ_{high}	<u>Maximum AOT first guess value</u>	<u>0,100</u>	<u>0,100</u>
$\sigma_{bb,FE}$	<u>Fine mode prior uncertainty for the AOT</u>	<u>1,0</u>	<u>1,0</u>
$\sigma_{bb,TC}$	<u>Coarse mode prior uncertainty for the AOT</u>	<u>2,0</u>	<u>2,0</u>
$\sigma_{bb,RPV}$	<u>Default prior uncertainty for the RPV parameters</u>	<u>1,0</u>	<u>1,0</u>

250 3.2 Aerosol vertices

Solution space for the wavelength $0.6\mu\text{m}$ defined by the non-absorbing fine mode (FN), the absorbing fine mode (FA) and the coarse mode (C) vertices. The red, green and blue lines show respectively the 99.7%, 95% and 68% probability regions respectively, as derived from AERONET inversion product for all the observations available over all the AERONET stations.

255 The choice of the aerosol vertices ~~determines the solution space in which~~ subsamples the entire solution space to a region where the aerosol properties can be retrieved. The relationship between the particle size and the single scattering properties has been discussed in Part I. As recommended ~~in the latter~~, three vertices are selected, defined by the asymmetry factor g and the Single Scattering Albedo (SSA) ω_0 : two fine mode vertices, absorbing and non-absorbing, and one coarse mode vertex, defining a triangle in the $[g, \omega_0]$ space in each processed band. The three vertices are chosen analysing the
 260 single scattering properties derived from the AERONET inversion product on all available observations since 1993 (Dubovik et al., 2006), similarly to the approach proposed by Govaerts et al. (2010). The aerosol single scattering properties distribution in the $[g, \omega_0]$ space, as derived from AERONET inversion product, is shown in Fig. 4 for $\lambda = 0.6\mu\text{m}$. ~~It can be seen that the~~ The aerosol properties
 265 are clustered in the region defined by $0.60 < g < 0.80$ and $0.85 < \omega_0 < 0.98$, containing 68.3% of the data (blue line). The selected CISAR vertices defining the solution space cover about the ~~90~~80% of possible solutions (~~magenta line~~)-black triangle).

4 Information content

~~Distribution of the Jacobians related to the RPV parameters. These distributions are obtained from~~

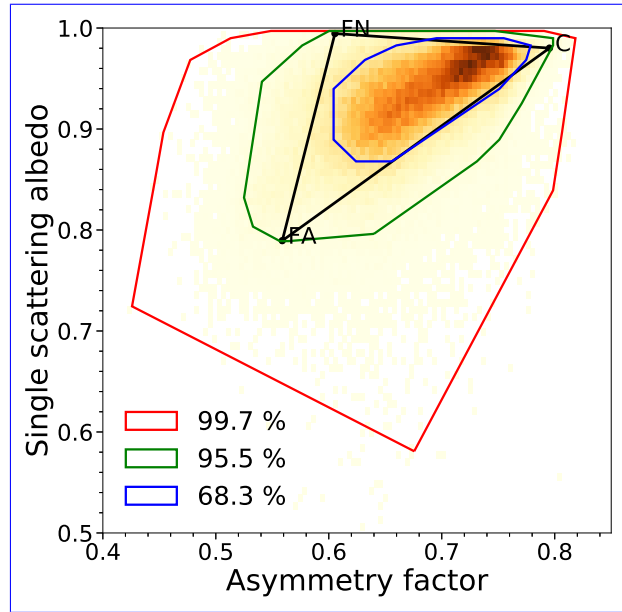


Fig. 4: Solution space (black triangle) for the wavelength $0.6 \mu\text{m}$ defined by the non absorbing fine mode (FN), the absorbing fine mode (FA) and the coarse mode (C) vertices. The red, green and blue lines show the 99.7%, 95.5% and 68.3% probability regions respectively, as derived from AERONET inversion product for all the observations available over all the AERONET stations.

270 ~~PROBA-V observations (RED band) over Carpentras, France (vegetated target).~~

The analysis of the information content relies on a two-fold approach. First, the Jacobians are used as an indicator of the TOA BRF sensitivity to state variable changes under different observation conditions. Next, the entropy is used as a rigorous metric to determine the information content of the observation system for each radiometer. The Jacobians, *i.e.*, the partial derivatives of the forward model with respect to the state variables, are affected by the changes in illumination and viewing geometry both in terms of sign and magnitude (Luffarelli et al., 2016). ~~Representing the sensitivity of the TOA BRF on the state variables, the Jacobians are a key parameter in the inversion process. The latter consists in fact in the~~ The minimisation of the cost function, ~~defined by Eq. 16 of Part I. This minimisation~~ relies on an iterative approach where the ~~descent direction~~ direction of steepest descent is determined by the Jacobians (Marquardt, 1963). An ~~intuitive~~ analysis of the Jacobians gives ~~a first insight into information about~~ the amount of information carried by the observation and the challenges associated to its sign and magnitude variations throughout the year, ~~both in term of sign and magnitude. The higher.~~ The larger the magnitude of the Jacobians, the higher the sensitivity of the signal on the selected state variable. ~~The Jacobians have been scaled by the variability range of each state variable to compare their dimensionless magnitude.~~

An illustrative example of the distributions of the Jacobians ~~related relative~~ to the RPV parameters is shown in Fig. 5 (~~Carpentras, France~~). ~~It can be seen that the~~ The Jacobians are dominated by the ρ_0 parameter (controlling the magnitude of the surface BRF), followed by θ , k and ρ_c (characteris-

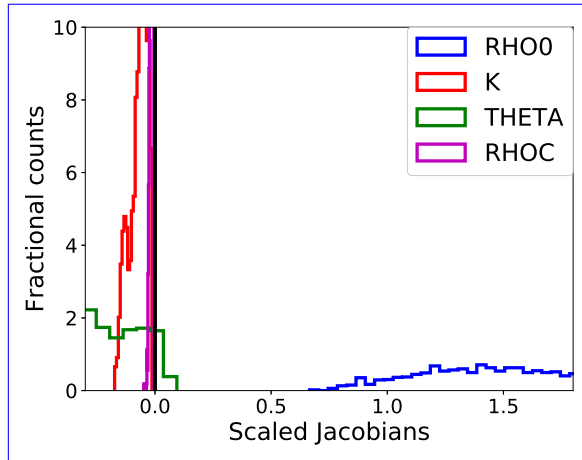


Fig. 5: Histograms of the distribution of the Jacobians related to the RPV parameters (x-axis), scaled by the variability range of each variable. These distributions are obtained from PROBA-V observations (RED band) over Carpentras, France (vegetated target). Positive (negative) values of the Jacobian show that the TOA BRF is positively (negatively) correlated to the considered state variable.

ing the surface reflectance anisotropy). Consequently, the retrieval of the surface reflectance shape
 290 ~~results more challenging with respect to~~ is more challenging than the retrieval of its mean magni-
 tude; nevertheless, its accurate retrieval is necessary to correctly account for the coupling between
 the surface and the atmosphere (Govaerts et al., 2008).

~~AOT Jacobians timeseries over Carpentras, France (vegetated target) related to SEVIRI VIS0.6
 band (top panel) and PROBA-V RED band (bottom panel) observations. The magenta dots represent
 295 the fine mode, the yellow triangles the coarse mode. — AOT Jacobians associated to SEVIRI~~

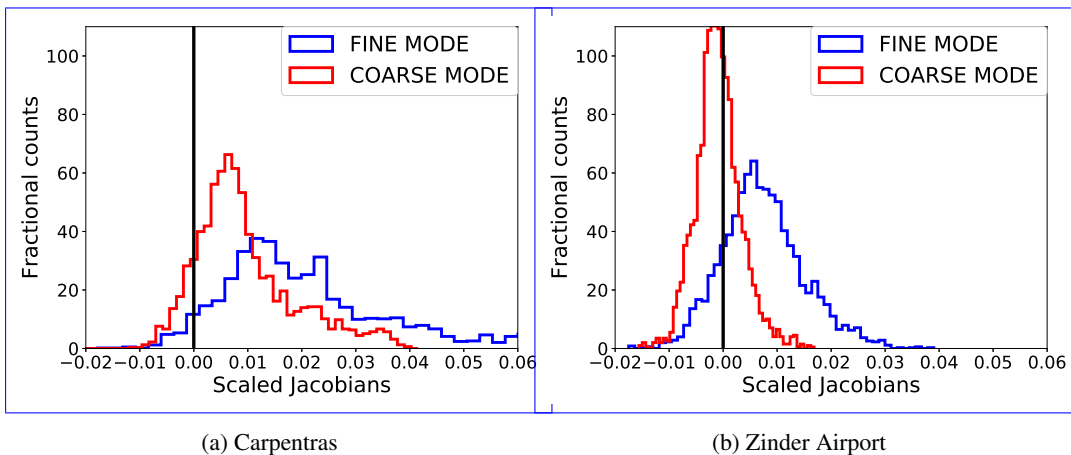
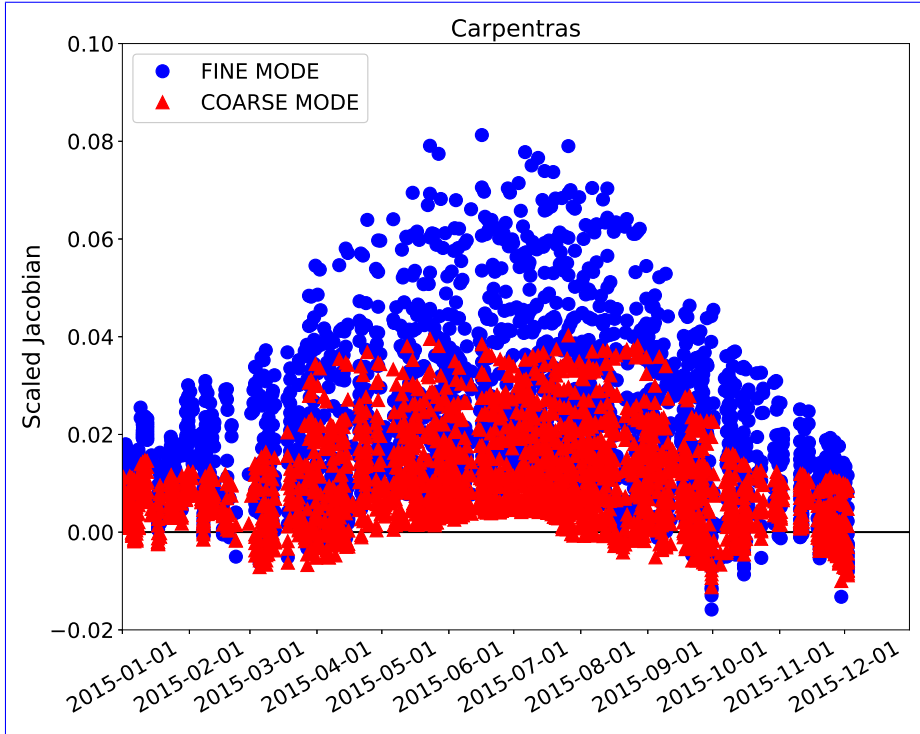
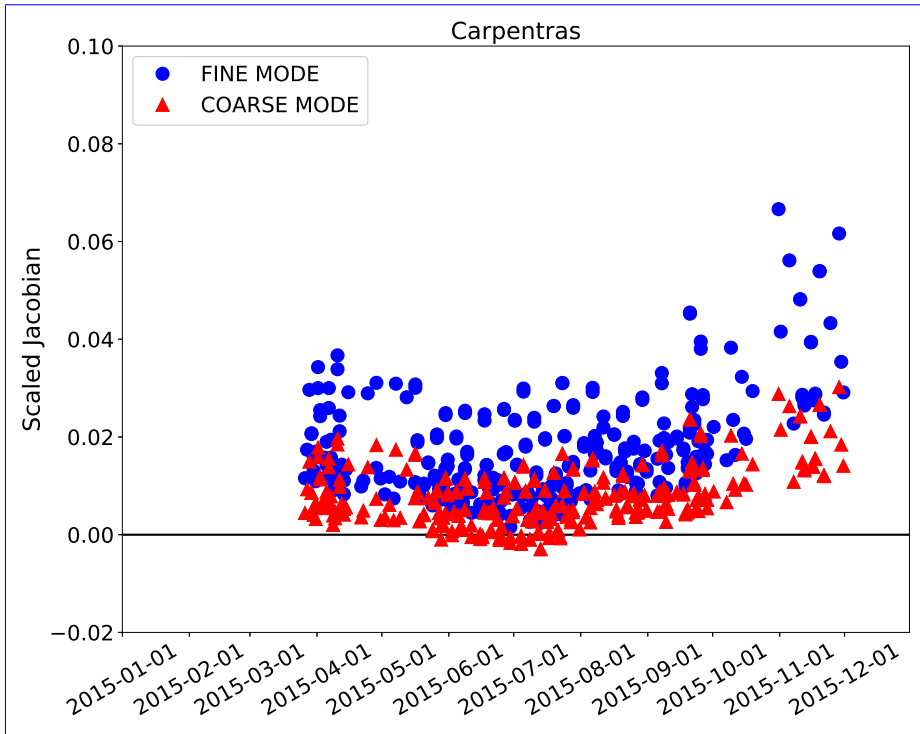


Fig. 6: Distribution of the AOT scaled Jacobian over Carpentras (dark surface) and Zinder Airport (bright surface). The histograms are obtained from PROBA-V observations (RED band) over year 2015.



(a) SEVIRI



(b) PROBA-V

Fig. 7: Median and standard deviation of state variables Scaled AOT Jacobians —The table refers timeseries over Carpentras, France (vegetated target) related to all processed targets during 2015. The values are shown for the SEVIRI SEVIRI VIS0.6 band (top panel) and PROBA-V bands centred at $0.6 \mu\text{m}$ RED band (bottom panel) observations. The blue dots represent the fine mode, the red triangles the coarse mode.

Table 9: Median and standard deviation of the scaled Jacobians. The table refers to all processed targets during 2015. The values are shown for the SEVIRI and PROBA-V bands centred at 0.6 μm .

	Median value	Standard deviation
ρ_0	<u>-1.410</u> <u>-1.316</u>	<u>0.7580</u> <u>0.385</u>
κ	<u>-0.065</u> <u>-0.008</u>	<u>0.0790</u> <u>0.038</u>
θ	<u>-0.148</u> <u>-0.250</u>	<u>0.2000</u> <u>0.265</u>
ρ_c	<u>-0.033</u> <u>-0.023</u>	<u>0.0310</u> <u>0.023</u>
τ_F	<u>0.088</u> <u>0.017</u>	<u>0.1350</u> <u>0.014</u>
τ_C	<u>0.035</u> <u>0.007</u>	<u>0.0700</u> <u>0.008</u>

~~observation over Carpentras, France, for 2015/6/5. The magenta dots represent the fine mode, the yellow triangles the coarse mode.~~

The aerosol contribution to the ~~signal at the satellite~~ TOA BRF differs according to the brightness of the surface. Figure 6 shows the AOT scaled Jacobians distribution over Carpentras (dark surface) and Zinder Airport (bright surface). ~~It can be seen that the~~ The Jacobians over Carpentras reach higher values with respect to the Jacobians related to Zinder Airport, ~~where the signal coming from~~ because the signal at Zinder is dominated by the bright surface ~~is larger with respect to dark targets~~ (Sun et al., 2016). When the magnitude of the AOT Jacobian is close to 0, the observed TOA BRF is not sensitive to changes in the aerosol concentration in the atmosphere. It is worth noticing that the ~~aerosol~~ AOT scaled Jacobians can be both negative and positive, meaning that the aerosols can increase or decrease the TOA BRF depending on the season and the viewing and illumination geometry. ~~The sign of the partial derivatives describes in fact in which way the state variables contribute to the signal. For instance, if the partial derivative of the TOA BRF with respect to the AOT is positive (negative), an increase in the aerosol concentration will increase (decrease) the signal.~~ This variability of the sign of the ~~Jacobian~~ Jacobians, occurring also over dark target, ~~as shown in~~ (Fig. 6a, ~~represent~~), represents one limitation in the MODIS Dense Dark Vegetation (DDV) algorithm (Kaufman et al., 1997), which assumes that an increase in the AOT results in an increased signal at the satellite, ~~this approach can only handle positive Jacobian values.~~

Table 9 shows ~~median values and standard deviation~~ the median value and the standard deviation of the scaled Jacobians for all the state variables at SEVIRI and PROBA-V bands centred at 0.6 μm , over all selected AERONET stations ~~over year 2015. This Table.~~ This table confirms the previous findings on the Jacobians magnitude shown in Fig. 5 and 6 over Carpentras and Zinder Airport. The AOT scaled Jacobian is about 2 orders of magnitude smaller than the one of the magnitude of the surface reflectance. The variability of the Jacobian sign and magnitude along the year is illustrated in Fig. 7, where it can be seen that the effect of the aerosols on the reflectance can vary with the geometry for the same land cover type. The Jacobian variations in Fig. 7 essentially depend on the viewing and illumination geometry. Aerosol particles mostly scatter in the forward direction, given the positive sign of the asymmetry factor g (controlled, among other factors, by the aerosol

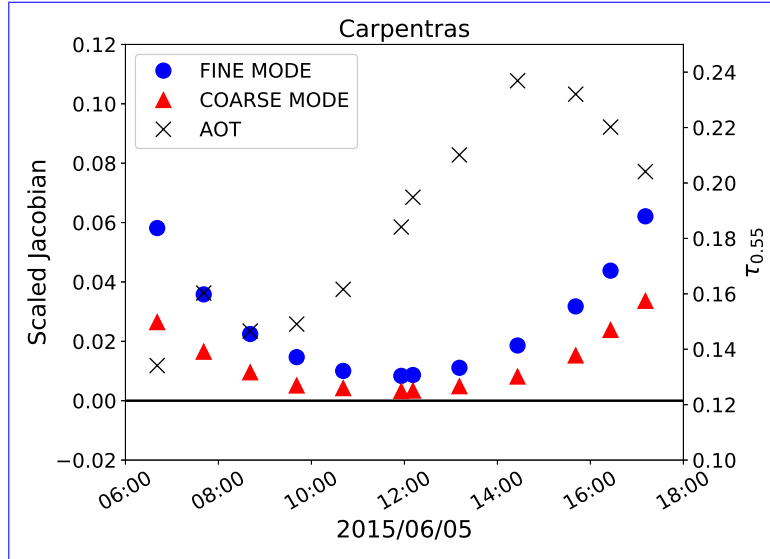


Fig. 8: Scaled AOT Jacobians (left y-axis) associated to SEVIRI observation in the VIS0.6 band over Carpentras, France, for 2015/6/5. The blue dots represent the fine mode, the red triangles the coarse mode. The black crosses represent the retrieved AOT at $0.55 \mu\text{m}$ (right y-axis).

The interpretation of the Jacobians allows an intuitive understanding of the sensitivity of the TOA BRF at the satellite with respect to the state variables. On the other hand, a

size distribution (Andrews et al., 2006). For this reason, the maximum information on the aerosols is located in the forward direction, while it decreases when approaching the backscattering direction. Additionally, a longer atmospheric path increases the aerosol effects on the reflectance, given the higher probability of interactions between the reflected sunlight and the atmospheric particles. The impact of the length of the atmospheric path is highlighted in Fig. 8, showing the Jacobian daily cycle over Carpentras. The sensitivity of the TOA BRF with respect to the AOT almost disappears at noon, when the atmospheric path is shortest and the signal coming from the surface is dominant with respect to the aerosols. The above considerations on the Jacobian have shown that the dominant contribution to the TOA BRF comes from the ρ_0 parameter, controlling the surface reflectance magnitude. The retrieval of the anisotropy of the surface appears to be more challenging, given the low dependency of the TOA BRF on it. This in turn makes the retrieval of the AOT challenging, given the radiative coupling between the atmosphere and effect of the aerosols on the anisotropy of the underlying surface (Wagner et al., 2010). Also, given signal is minimised. A more detailed analysis of the AOT Jacobians and their relation with the AOT magnitude is performed by Luffarelli et al. (2016). Given the seasonal variations of the Jacobian, it is not easy to have expected to get the same accuracy of the retrieval throughout the day and throughout the year.

A more rigorous analysis of the information content can be made through the entropy, the measure of the which measures the uncertainty reduction (Rodgers, 2000). In an OE framework,

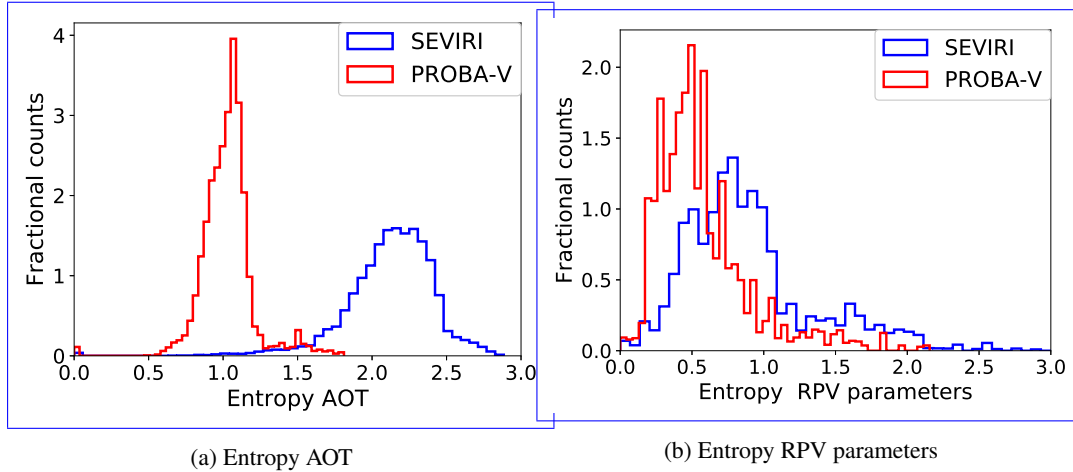


Fig. 9: ~~Same as Figure ?? but~~ Distribution of the entropy related to the ~~surface space~~ AOT (left panel) and to the RPV parameters (right panel).

the prior information and its uncertainty represent an hypothesis on the expected value of the state variables. It is envisaged that the inversion process provides a posterior uncertainty on the state variables which is smaller than the prior one; the entropy quantifies this uncertainty reduction. When there is no information coming from the satellite observations, the entropy will be close to 0 as the observation does not add any additional knowledge on the system. Formally, the entropy is computed as follows:

$$H = -\frac{1}{2} \ln \left(\frac{|\mathbf{S}_{\hat{x}}|}{|\mathbf{S}_x|} \right) \quad (10)$$

where $\mathbf{S}_{\hat{x}}$ ~~is the uncertainty of the posterior~~ (Eq. 21 of Part I) and \mathbf{S}_x ~~is the uncertainty of the prior information.~~ are the uncertainties of the posterior and the prior information respectively. Distribution of the entropy related to the aerosols properties for SEVIRI (left panel) and PROBA-V (right panel) respectively.

345 In CISAR, the entropy is calculated ~~for the RPV parameters and the AOT separately;~~ its considering the surface and atmospheric state variables and their associated prior and posterior uncertainty separately; the entropy distribution is shown in Fig. ~~?? and ?? respectively.~~ As it can be observed the 9. The distribution of the surface and AOT entropy related to SEVIRI observations exhibits higher values compared to the one related to PROBA-V observations, meaning a
 350 higher information content from geostationary satellites observations with respect to polar orbiting ones, especially for the AOT. It should be noticed that the given the larger radiometric uncertainty associated to the observations acquired by the polar orbiting satellite. The entropy depends not only on the information carried by the satellite observation, but also on the uncertainty associated to the prior information. As the prior information on the surface is updated as in Section 2.4, the
 355 uncertainty associated with it (Sect. 2.4), the associated uncertainty decreases in time, whereas the prior information on the AOT remains weakly constrained, as the uncertainty is kept to the default

high value. ~~This is the reason why~~ For this reason the entropy associated to the RPV parameters (Fig. ??) exhibits smaller value than the one associated to the AOT (Fig. ??). ~~Geostationary satellites acquire observations at a higher temporal frequency than polar orbiting one; the multi-angular vector obtained by accumulating satellite observations over time will thus offer a larger and more diverse angular sampling with respect to polar orbiting satellite observations (Fig. 3). This, in turn, results in a higher probability of correctly characterising the surface anisotropy and its coupling with the atmosphere (Wagner et al., 2010). 9a).~~

5 Quality indicator

5.1 ~~Principle~~ Review of existing methods

~~In Section 2.5 the OE assumption~~ Section 2.5 discussed the limitations of the forward model being capable of correctly characterising the satellite observation has been discussed. However the CISAR forward model, FASTRE, described in Part I, is a simple 1D model which is not always capable of fitting the complexity of the observations FASTRE. Furthermore, in ~~Section Sect.~~ 4 it has been shown how the AOT Jacobian magnitude is subject to ~~daily and seasonal variation~~ temporal variations, depending on the viewing and illumination ~~geometry~~ geometries. These issues compromise the reliability of the retrieved solution, which can however be assessed using different methods. Dubovik et al. (2011) use the relative fitting measurement residual, ~~the observation term of the cost function~~, to filter the retrieval outliers. Such an approach presents some limitations as the ~~probability to have a good fit by chance increases as the numbers of cloud-free observations decreases.~~ number of degrees of freedom can vary depending on the availability of cloud free observations. The requirement on the quality of the fit should be stricter when only a limited number of observations is available (Govaerts et al., 2010). To address this specific issue, Govaerts and Lattanzio (2007) developed an approach ~~based on the residual of the cost function, but also taking~~ which also takes into account the number of cloud free observations. The authors observed that the ~~latter can vary between pixels, and that the~~ cost function is proportional to the quadratic sum of the ~~miss-fit~~ mismatch between the simulation and the observation for each acquisition, weighted by the observation uncertainty. ~~For these reasons, as~~ As the cost function is strongly dependent on the number of observations, it is not possible to define a universal range of acceptable values for its residual ~~:-~~

~~Correlation (in purple) and RMSE (in blue) variations in function of the miss-fit test p_3 . The figure refers to the CISAR AOT retrieval evaluation against AERONET data. These results are obtain from CISAR applied to SEVIRI observations. Nevertheless, both~~ without performing additional operations on the cost function. Both methods do not correctly identify situations in which a good fit ~~of the TOA BRF~~ is reached but the retrieval of the state variables is not reliable, due to limited or no dependency of the TOA BRF on the state variables ~~;-~~ (the Jacobians are close to θ . ~~A more elaborated~~ 0). A more elaborate QI has been developed for the MODIS Aerosol Product Collection

6 (Hubanks, 2017), which is composed of different tests accounting for the fitting residual, the magnitude of the retrieved AOT, the possible presence of cirrus, the brightness of the scene and ~~informations~~ information on the number of pixels and the percentage of water pixels present in the processed area. Despite taking into account different factors in addition to fitting residuals, this approach does not consider the actual information content of the satellite observation. Moreover, as CISAR ~~performs the retrieval on a pixel-level~~ processes each pixel independently, the information on the number and type of pixels over which the retrieval is performed, as used in the MODIS product, is not applicable within this method.

400 5.2 Overview

A new approach is ~~therefore proposed here~~ proposed for the CISAR algorithm, which combines a series of individual tests ~~p_i to defined j with an associated value p_j in the range $[0,1]$, defining a $QI(t_i)$ associated to each retrieved solution~~ the solution retrieved at the time t_i . The proposed method takes into account These tests are performed on the convergence of the inversion to a solution after a given number of iterations (~~p_0), 0), on the validity range of the total AOT (~~p_1) and surface albedo (p_2), the miss-fit 2), on the mismatch~~ between observations and simulations (~~p_3) and 3) and on the information content of the satellite acquisition through the Jacobians (~~p_4) and the entropy, as discussed in Section Sect. 4. The entropy is computed separately for the AOT (~~p_5) and RPV parameters (~~p_6)~~~~~~~~. These tests have been defined ~~through~~ through an analysis of their impact on the CISAR performance when evaluated against independent datasets (see Supplement) reference datasets. The value p_j associated to each test can assume values between 0 (bad quality) and 1~~

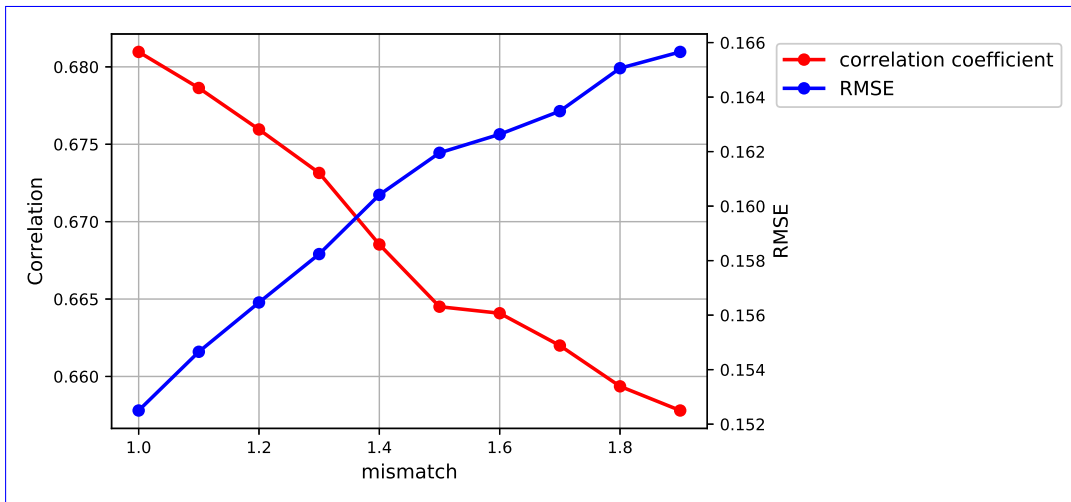


Fig. 10: Correlation (in red) and RMSE (in blue) variations in function of the mismatch between the satellite observation and the simulated signal (test 3). The figure refers to the CISAR AOT retrieval evaluation against AERONET data. These results are obtain from CISAR applied to SEVIRI observations.

(good quality). Figure 10 shows an example of the ~~retrieved AOT evaluation against evaluation of the retrieved AOT against the~~ AERONET data for the ~~miss-fit test (p_3); it can be seen that a better fit leads to a smaller RMSE and a higher correlation mismatch test (3). As the mismatch increases,~~
 415 ~~the correlation decreases, while the Root Mean Square Error (RMSE) shows opposite behaviour.~~

5.3 ~~Theoretical concept~~ Quality indicator tests

5.3.1 Convergence

The first ~~tests test~~ to be performed is on the convergence of the inversion ~~p_0 ; when~~. When the maximum number of iteration is reached, ~~the entire processed accumulation period is assigned a QI equal to 0. The convergence is the first parameter to be analysed because if this test fails,~~ CISAR ~~has not actually converged to a solution, the other tests are not performed.~~ ~~p_0 is equal to 0, otherwise $p_0 = 1$.~~

5.3.2 State variable validity range

The validity of the retrieved total AOT ~~p_1~~ and of the surface BHR ~~p_2 is investigated. In fact is~~
 425 ~~examined in the tests 1 and 2. In CISAR, a validity range for each state variable is defined, based on physical boundaries and empirical observations. When the retrieved state variable is equal to the minimum or maximum value determining value of retrieved AOT (BHR) falls on the extremes of this range, a QI=0 is assigned to the retrieval. The minimum and maximum values defining the AOT and BHR validity range are reported in Table ??.~~ Normally, very high values of AOT (close to 5.0)
 430 ~~indicates cloud contamination. Validity range for the total AOT and BHR: Min Max p_1 (p_2) is equal to 0. The acceptable values for the BHR 0.0-1.0 AOT 0.0-5.0 range from 0 to 1, while the AOT can only assume positive values smaller than 5. The values p_1 and p_2 are equal to 1 when $0 < BHR < 1$ and $0 < AOT < 5$ respectively.~~

5.3.3 ~~Miss-fit~~ Mismatch between observation and simulation

As discussed in ~~the Section~~ Sect. 5.1, the fitting residual between the observation and the simulation is normally used to assess the reliability of the solution, as it describes if how well the signal simulated with the forward model ~~correctly characterise~~ ~~$y_m(t_i, \lambda)$ fits~~ the satellite observations. ~~The miss-fit $y_o(t_i, \lambda)$. The mismatch~~ between the observed and simulated TOA BRF is ~~evaluated in terms of weighted by~~ the observations uncertainty :-

$$p_3(t) = \frac{|y_m(t) - y_o(t)|}{\sigma_o(t)}$$

435 ~~where $y_m(t)$ is the BRF calculated by the forward model at time t , $y_o(t)$ is the observation and $\sigma_o(t)$ is the observation uncertainty. As anticipated in Section 2.1 the observation uncertainty plays~~

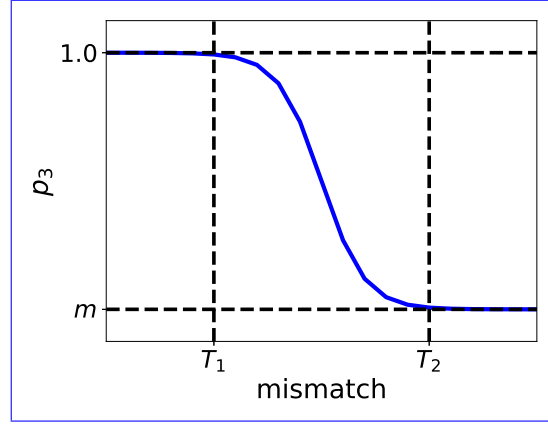


Fig. 11: Non linear p_3 definition between the minimum value m and 1 which applies when the mismatch is larger than T_1 and smaller than T_2 .

a fundamental role in the minimisation problem, appearing as denominator in the cost function observation term (Eq. 17 Part I). For the inversion being successful, the difference between the $\sigma_0(t_i, \lambda)$. For this test, the largest mismatch among the processed bands is considered. Two thresholds T_1 and T_2 are defined to identify good ($p_3 = 1$) and bad ($p_3 = 0$) quality retrievals. The difference between the simulated signal and the satellite observation should be entirely justified by the observation uncertainty $\sigma_o(t)$, it should results $p_3(t) \leq 1$ satellite observation should have the same magnitude as the observation uncertainty $\sigma_0(t_i, \lambda)$, therefore the T_1 is set to 1. Conversely, the maximum acceptable mismatch value $T_2 = 2$ has been chosen observing the relation between the mismatch and the performances of CISAR when evaluated against the independent datasets used as reference. Fig. 10 represents an example of this analysis. When the mismatch assumes values within the range defined by T_1 and T_2 , thresholds included, a value between a minimum m and 1 is assigned to p_3 through a sigmoid function with width equal to $10/(T_2 - T_1)$ (Fig. 11). A different coefficient m is defined for each test j in order to give different weights to the tests, according to the magnitude of their impact on the retrieved solution and its evaluation against the reference dataset. The outcome of the test 3 is thus defined as follows:

$$\begin{cases} p_3(t_i) = 0 & \text{if } \max_{\lambda} \left\{ \frac{|y_m(t_i, \lambda) - y_0(t_i, \lambda)|}{\sigma_0(t_i, \lambda)} \right\} > T_2 \\ p_3(t_i) = 1 & \text{if } \max_{\lambda} \left\{ \frac{|y_m(t_i, \lambda) - y_0(t_i, \lambda)|}{\sigma_0(t_i, \lambda)} \right\} < T_1 \\ m < p_3(t_i) < 1 & \text{if } T_1 \leq \max_{\lambda} \left\{ \frac{|y_m(t_i, \lambda) - y_0(t_i, \lambda)|}{\sigma_0(t_i, \lambda)} \right\} \leq T_2 \end{cases} \quad (11)$$

with $\lambda=1, \dots$ number of wavelengths.

5.3.4 Jacobian Jacobians

As discussed in Section 4, the Jacobians give information on the sensitivity of the TOA BRF on the state variables. Performing a test over the Jacobians magnitude on the Jacobians related to each state variable might however can be computationally expensive. To In order to reduce the computational effort, only the Jacobian of the AOT is taken into account. This choice derives from the analysis of the Jacobian distributions related to the retrieved state variables, which median values and standard deviations are reported in Table 9. It can be observed that the surface anisotropy parameter κ , the fine and coarse mode AOT and the hotspot parameter ρ_c present low Jacobian magnitude with a small standard deviation. However, Maignan et al. (2003) evaluated the impact of a correct hotspot modeling on the surface albedo estimate. They found that, being limited to a small angular range, the impact of the hotspot effect on the albedo is negligible. For this reason, it has been chosen to discard the analysis of the ρ_c Jacobian for the QI computation. Additionally, the surface prior update mechanism described in Section 2.4 provides a robust estimate of the surface BRF parameters. Hence, only the AOT Jacobians are considered for the elaboration of the QI. Moreover, the spectral constraints applied on the AOT variability as in Section Sect. 2.4 impose a correlation between the AOT retrieved in the different spectral bands. Consequently, it is desirable to have information large absolute Jacobians in at least one band, but this information has to be present in each aerosol vertex in order to have. To have a good retrieval of the total AOT. Hence, the parameter considered in this quality assessment is computed as follows, the AOT associated to each aerosol vertex has to be correctly retrieved. The quantity $\hat{K}_x(t_i)$ analysed in the test 4 is thus the following:

$$p_4 \hat{K}_x(t_i) = \max_{\lambda} \left\{ \min_v \left\{ J_{\tau_{\lambda,v}} |K_{x_{\lambda,v}}(t_i)| \right\} \right\} \quad (12)$$

where with $\lambda=1, \dots$, number of wavelengths and $v=1, \dots$, number of aerosol vertices.

The aim of this test is to discard observations with little or no sensitivity to the AOT, identifying those situations where the test on the miss-fit is successful because of the prior information and/or the temporal and spectral constraints (Sect. 2.1) rather than actual information coming from the observations. The thresholds T_1 and T_2 are set to 0.01 and 0.02 respectively. The values of p_4 are defined similarly to p_3 :

$$\begin{cases} p_4(t_i) = 0 & \text{if } \hat{K}_x(t_i) < T_1 \\ p_4(t_i) = 1 & \text{if } \hat{K}_x(t_i) > T_2 \\ m < p_4(t_i) < 1 & \text{if } T_1 \leq \hat{K}_x(t_i) \leq T_2 \end{cases} \quad (13)$$

5.3.5 Entropy

Section 4 discusses how the entropy, quantifying the entropy computation as a rigorous analysis of the information content, quantify the uncertainty reduction from the prior knowledge on the

system to the posterior uncertainty ~~after the inversion. This test analyses separately the entropy related~~, represents a rigorous analysis of the information content. Tests 5 and 6 analyse the entropy associated to the AOT (p_5) and the RPV parameters (p_6), compute and the one associated to the RPV parameters, computed as follows:

$$\begin{aligned} H_{AOT}(t_i) &= -\frac{1}{2N_\lambda} \ln \left(\frac{\prod_\lambda \prod_v \sigma_{post}(t_i, \lambda, v)}{\prod_\lambda \prod_v \sigma_{prior}(t_i, \lambda, v)} \right) \\ H_{RPV}(t_i) &= -\frac{1}{2N_\lambda} \ln \left(\frac{\prod_\lambda \prod_p \sigma_{post}(t_i, \lambda, p)}{\prod_\lambda \prod_p \sigma_{prior}(t_i, \lambda, p)} \right) \end{aligned} \quad (14)$$

where N_λ is the number of processed wavelengths, $\lambda=1, \dots, N_\lambda$, $p=1, \dots$, number of RPV parameters and $v=1, \dots$, number of aerosol vertices. The normalization to N_λ assures consistency in the entropy evaluation when different number of bands are analysed, as for SEVIRI and PROBA-V cases.

490 5.4 Quality indicator computation

The final QI is computed combining the results of the tests performed on the retrieved solution. As described in Section 5.3.1 and 5.3.2 a QI equal to 0 is assigned if one test among p_0 , p_1 and p_2 fails. For the quantities p_i , with $i=3 \dots 6$, a minimum $T_{1,i}$ and a maximum $T_{2,i}$ thresholds are defined to discriminate between good and poor quality retrievals and a intermediate indicator q_i is assigned as follows:-

$$\left\{ \begin{array}{l} q_i = 0 \quad \text{if } p_i(t) \leq T_{1,i} \quad \forall \quad i = 4, 5, 6 \quad \text{or} \quad p_i(t) \geq T_{2,i} \quad \forall \quad i = 3 \\ q_i = 1 \quad \text{if } p_i(t) \geq T_{2,i} \quad \forall \quad i = 4, 5, 6 \quad \text{or} \quad p_i(t) \leq T_{1,i} \quad \forall \quad i = 3 \\ m_i < q_i < 1 \quad \text{if } T_{1,i} \leq p_i(t) \leq T_{2,i} \quad \forall \quad i = 3, 4, 5, 6 \end{array} \right.$$

where m_i is the minimum value assigned to q_i . These weights are selected according to the principle behind the test i definition and the different impact that the different quantities p_i have on the fitting between the CISAR retrieval when evaluated as explained in Section 5.1. For instance, a larger weight is given to the test on the miss-fit, q_3 , as it indicates whether the forward model was capable of correctly simulated the observation, this being one of the main assumption of the OE method. The entropy computation is strongly dependent on the magnitude of the prior uncertainty as explained in Section 2.5. When $T_{1,i} \leq p_i(t) \leq T_{2,i}$ the value of q_i is determined non-linearly through a sigmoide function as in Fig. 11. In fact, as the quality of the retrieval does not change rapidly moving away from the thresholds $T_{1,i}$. Sect. 4. Low entropy might be due to reliable prior information, with a low associated uncertainty. Similarly, the uncertainty reduction would be very large in case of little prior information on the state variable. For these reasons, tests 5 and $T_{2,i}$, the smoother transition obtained with a sigmoide function has been preferred to a linear transformation.

Non-linear q_i definition between a minimum m_i and 1 which applies for the parameter p_i when

510 $T_{1,i} \leq p_i(t) \leq T_{2,i}$.

Finally, the $QI(t)$ associated with each retrieval t is computed as follows:-

$$QI = p_0 p_1 p_2 \left(1 - \max \left\{ \sum_{i=3}^6 (1 - q_i), 0 \right\} \right)$$

Correlation (in purple) and RMSE (in blue) variations in function of the QI. The figure refers to the CISAR AOT retrieval from SEVIRI (top panel) and PROBA-V (bottom panel) observations evaluated against AERONET data.

The selection of the thresholds $T_{1,i}$ and $T_{2,i}$ results from the *a posteriori* evaluation of the CISAR retrieval against independent datasets as in Section 5.1 and based on the meaning of each test i . For instance, $T_{1,3}$, the minimum threshold related to the miss-fit between observed and simulated TOA BRF test, is set to 1, as $p_3 \leq 1$ means that the difference between the simulated signal and the satellite observation does not exceed the observation uncertainty σ_o . Conversely, $T_{2,3}$ has been chosen observing the impact of p_3 on the fitting between CISAR retrieval and the independent datasets used as reference (Fig. 11 represents an example of this evaluation). T_2 has thus been set to 2.0, meaning that the maximum tolerance on the miss-fit is equal to $2\sigma_o$. Regarding the test on the Jacobian magnitude, its aim is to discard observations with Jacobians close to 0, where there is little or no dependency of the TOA BRF on the AOT rather than associate a large Jacobian to a good quality retrieval. In other words, this test intends to identify those situations where the test on the miss-fit is successful because of the prior information and/or the temporal and spectral constraints (Section 2.1) rather than actual information coming from the observations. The thresholds $T_{1,4}$ and $T_{2,4}$ are therefore set to 0.01 and 0.02 respectively, in order to filter out observations where the Jacobian magnitude is close to 0. Finally, the tests performed on the entropy are strongly dependent on the magnitude of the prior uncertainty as explained in Section 4. For this reason an additional step is performed on p_5 and p_6 , they are only performed when the prior uncertainty is smaller than the validity range of the AOT and RPV respectively and larger than 1/6 of it. The thresholds associated to the two tests on the entropy are $T_{1,5} = T_{1,6} = 0.1$ and $T_{2,5} = T_{2,6} = 0.6$. $T_1 = 0.1$ and $T_2 = 0.6$ that correspond to a 20% and 70% uncertainty reduction respectively. The values $p_5(t_i)$ and $p_6(t_i)$ are computed as in Eq. 15.

$$\begin{cases} p_{5,6}(t_i) = 0 & \text{if } H_{AOT}(t_i), H_{RPV}(t_i) < T_1 \\ p_{5,6}(t_i) = 1 & \text{if } H_{AOT}(t_i), H_{RPV}(t_i) > T_2 \\ m < p_{5,6}(t_i) < 1 & \text{if } T_1 \leq H_{AOT}(t_i), H_{RPV}(t_i) \leq T_2 \end{cases} \quad (15)$$

535 5.4 Quality indicator computation

The final QI is computed combining the results of the tests performed on the retrieved solution:

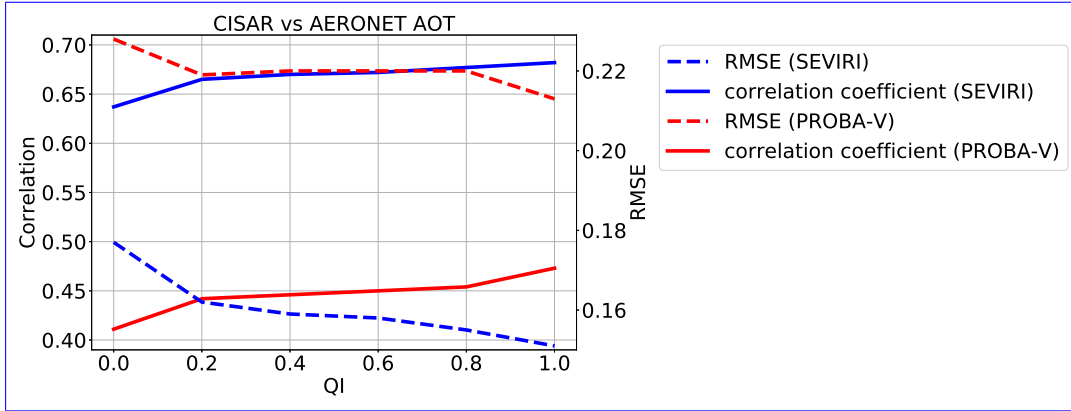


Fig. 12: Correlation (straight lines) and RMSE (dashed lines) variations in function of the QI. The figure refers to the CISAR AOT retrieval from SEVIRI (in blue) and PROBA-V (in red) observations evaluated against AERONET data.

$$QI(t_i) = p_0(t_i)p_1(t_i)p_2(t_i) \max \left\{ 1 - \sum_{j=3}^6 (1 - p_j(t_i)), 0 \right\} \quad (16)$$

The final $QI(t_i)$ ranges from 0 to 1, where 0 designate a poor quality retrieval and 1 indicates a reliable solution. Figure 12 shows the variations of the correlation and the RMSE between CISAR retrieved AOT and AERONET data as a function of the QI. Correlation increases as QI is taking large values larger values, while the RMSE decreases. This behaviour is observed with CISAR AOT retrieved from both SEVIRI (Fig. 12a) and PROBA-V observations (Fig. 12b) observations). This correlation increase (RMSE decrease) is particularly visible when QI is taking values between 0.0 and 0.2. For this reason, in Section 6 only retrievals with $QI \geq 0.2$ are considered in Sect. 6.

6 Performance evaluation

545 6.1 BHR

Table 10: CISAR retrieved BHR from actual observations comparison with MODIS in all the processed bands.

	SEVIRI			PROBA-V			
	$0.6 \mu\text{m}$	$0.8 \mu\text{m}$	$1.6 \mu\text{m}$	$0.4 \mu\text{m}$	$0.6 \mu\text{m}$	$0.8 \mu\text{m}$	$1.6 \mu\text{m}$
Number of points	7409			744			
Correlation	0.917	0.779	0.854	0.743	0.864	0.618	0.841
Root Mean Square Error	0.045	0.067	0.079	0.029	0.052	0.098	0.091
Mean Absolute Bias	0.039	0.067	0.067	0.025	0.045	0.070	0.077

The CISAR BHR, computed from the RPV parameters, is compared with the MODIS Land product (Schaaf and Wang, 2015). To account for the different spatial sampling, the MODIS data have been averaged on 5x5 km and 1x1 km for the comparison with the retrievals from SEVIRI and PROBA-V respectively. The results of this comparison are shown in Table 10 in terms of correlation, RMSE, and Mean Absolute Error (MAE). The CISAR results show a high correlation with the MODIS product, higher than 0.7 in all the processed spectral bands, except the PROBA-V NIR band, which shows a correlation equal to 0.618. The density plots of the CISAR BHR retrievals against MODIS data are included in the Supplement for all the processed bands, for both satellites. Despite the instrument differences discussed in Sect. 2.5, the CISAR retrievals and the MODIS Land Product dataset show similar seasonal trends. Figure 13 shows the BHR timeseries over Zinder Airport (Niger, Africa), as retrieved from the CISAR algorithm applied to SEVIRI and PROBA-V observations and from the MODIS Land Product. The rainy season, going from May 20 to October 5 (Weatherspark.com, 2018), is distinguishable through the decrease of the surface BHR in both the MODIS and CISAR datasets, although CISAR retrieves a larger seasonal variation with respect to MODIS product. The effect of the updating mechanism on the surface prior described in Sect. 2.4 is also visible as the retrieval uncertainty decreases in time, given that the prior information on the surface is better defined.

6.2 Aerosol Optical Thickness

The CISAR AOT retrieval, extrapolated at $0.55 \mu\text{m}$, has been evaluated against the AERONET data over the selected targets listed in Section 2. Sect. 2. The CISAR AOT retrieval is evaluated in terms of correlation, RMSE, ~~Mean Absolute Bias (MAE)~~ MAE with respect to AERONET values. Additionally, the percentage of points falling within the Global Climate Observation System (GCOS) requirements (Systematic Observation Requirements for Satellite-Based Data Products for Climate, 2011 Update), defined as $\max\{0.0300, 10\%\}$ ~~$\max\{0.03, 10\%\}$~~ , is also accounted for. The GCOS requirements are a useful tool to compare different algorithms' performances. However, ~~it should be considered that~~ both SEVIRI and PROBA-V missions were not originally designed for AOT retrieval, ~~whereas the GCOS requirements establish the standards~~. The GCOS requirement of 0.03 for low optical thickness translates into a radiometric noise requirement much better than 2 (1)% at 0.4 (0.6) μm , way below the radiometric performance of the SEVIRI and PROBA-V instruments (Table 3). The duration of the corresponding missions provides however a decisive advantage for the generation of ~~Essential Climate Variables (ECVs) derived from dedicated missions~~ AOT datasets from these instruments. In the following, the GCOS requirements are evaluated in terms of percentage of retrievals satisfying them. ~~The duration of the corresponding missions provides however a decisive advantage for the generation of AOT ECVs.~~

580 Fine (blue) and coarse (green) mode at $0.55 \mu\text{m}$ distributions from AERONET observations over the selected stations (Table 1) over year 2015.

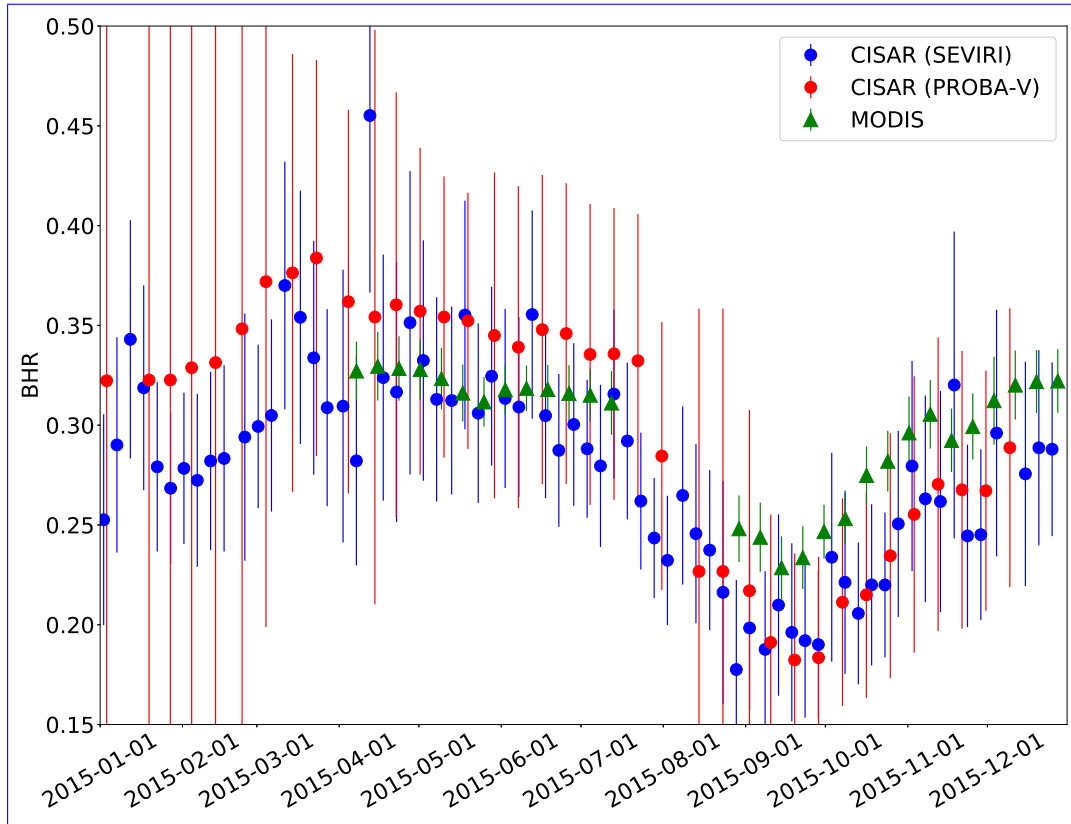


Fig. 13: CISAR retrieved BHR from SEVIRI (blue dots) and PROBA-V (red dots) and MODIS Land Product (green triangle) over Zinder Airport (Niger, Africa). The results are shown for the sensors band centred at $0.6 \mu m$, for year 2015. The vertical bars represent the retrieval uncertainty for SEVIRI and PROBA-V and standard deviation over the selected area for MODIS.

Figure 14 shows the evaluation of the retrieved AOT against AERONET data for both SEVIRI (left panel) and PROBA-V (right panel). ~~CISAR retrieval~~The CISAR retrievals from SEVIRI observations shows a better agreement with the AERONET data compared to the ~~retrieval~~retrievals from PROBA-V observations. This is in accordance with the poor radiometric performances of the polar orbiting instrument and with the outcome of the information content analysis performed in ~~Section 4.~~Sect. 4.

The boxplots in Fig. 14 show a slight an overestimation of the retrieval for low AOT ($\tau < 0.2$) and an underestimation for large AOT ($\tau > 0.6$). A similar behaviour is also observed in Wagner et al. (2010).

~~Example of possible cloud contamination from SEVIRI observations iver a 3x3 pixel window on the 24th of June over Burjassot, Spain. The upper panel show the CISAR retrieval (blue dots) and AERONET data (yellow triangles) over the central pixel. The bottom left and right panel show the TOA BRF and the cloud mask over the 3x3 pixel window respectively.~~ The underestimation for large values might be partially due to the temporal constraints described in ~~Section~~Sect. 2.4,

as they might prevent the algorithm to fit rapidly evolving aerosol events associated with large AOT values. However the applied temporal constraints are intended to optimise the retrieval of low aerosol concentration, given the global distribution of AOT which normally results is normally smaller than 0.2 (Kokhanovsky et al., 2007). A second possible explanation is related to the low Jacobians of the AOT, particularly the coarse mode. High AOT are in fact generally related to large particle (coarse mode) events (Fig.??). However, when the observation does not carry enough information, the CISAR algorithm relies on the prior information, this being an annual climatology value, hence normally lower than 0.2. Although the associated uncertainty is very large, the prior information still impacts the retrieved value. Some example of CISAR Additionally, very high AOT normally correspond to local events, especially in Europe (e.g. plume, fire), therefore the AOT obtained by the retrieval from the satellite pixel containing the AERONET station will be lower than the one measured by the AERONET tower (Jiang et al., 2007). The histograms in Fig. 14 show that AOT values larger than 0.8 represent less than 5% of the total number AERONET observations, affecting the reliability of the statistics for high values of AOT. The processing of more data would be necessary to increase the confidence in the results for high AOT values. Some examples of CISAR's ability to detect high AOT are shown in the Supplement. The overestimation for The overestimation of low AOT might originate from undetected or neighbouring clouds. Cloud

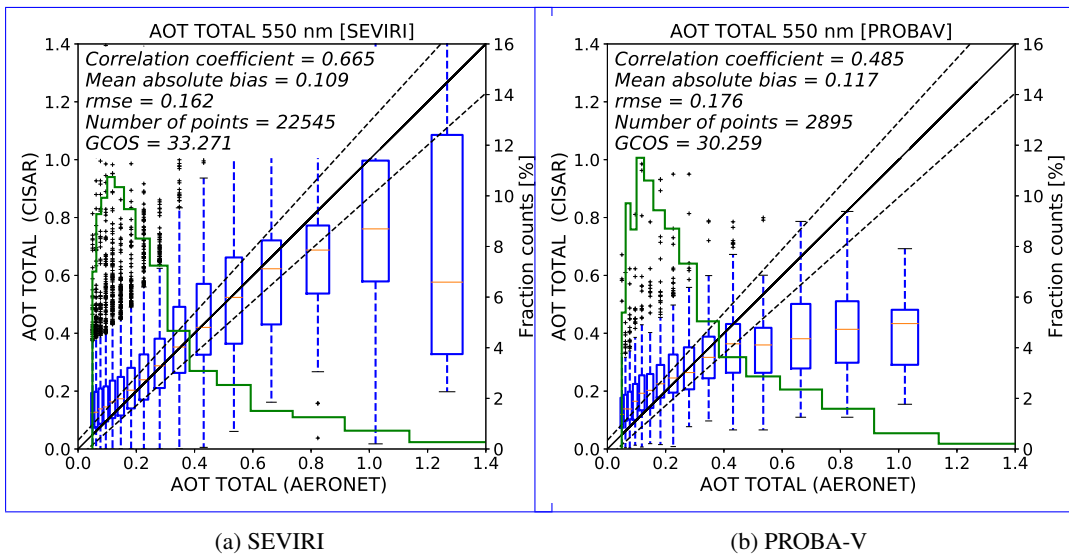


Fig. 14: Boxplot between Boxplots showing the CISAR total-AOT retrieval (extrapolated at 0.55 μm (left y-axis) and against the AERONET data (x-axis) for both SEVIRI (left panel) and PROBA-V (right panel) over all the selected stations in 2015. Only retrieval retrievals with $0.2 \leq QI \leq 0.2$ are considered. The blue boxes represent the interquartile range (IQR), the red horizontal line inside the blue boxes represents the median value, the vertical dashed bars represent the $1.5 \times IQR$ range and the black crosses represent the outliers. Boxes with less than 10 points are not displayed. The green histograms represent the AERONET AOT distribution. The right y-axis shows the percentage of points contained in each bin.

contamination can in fact be observed even few kilometres distant from clouds, increasing the AOT (Chand et al., 2012). Figure ?? shows an example of cloud contamination for the Burjassot AERONET station, Spain, for SEVIRI observations. Here the CISAR overestimation for low AOT values is clearly visible on June 24th. Figure ?? shows the TOA BRF and the cloud mask on a the different spatial scale between the satellite observations and the ground measurements. Most of the selected AERONET stations are located in Europe (Fig. 1), where the SEVIRI pixel resolution is about 5x8 km (as opposed to 3x3 pixels windows. The processed pixel is surrounded by cloudy pixels, probably leading to cloud contamination in the central pixel and consequently to the overestimation of the retrieval. Satellite measurements, being applied to pixels of few kilometers, are thus more likely to be affect by cloud contamination than ground observations . The probability to have pixels of that size contaminated by small undetected cloud could also explain this overestimation km at the subsatellite point), which is compared to AERONET point measurement. The probability of residual cloud contamination at this scale might thus explain part of the overestimation (Henderson and Chylek (2005), Chand et al. (2012)). Furthermore, the shortest SEVIRI spectral band is centred at $0.67 \mu\text{m}$, where the sensitivity to low optical thickness is about 2 times smaller than in the blue spectral region. Consequently, the retrieval in these cases essentially relies on the prior information regardless the very large associated uncertainty. Despite the presence of a blue band and a better spatial resolution (1 km), the retrievals from PROBA-V observations still show overestimation at low AOT, due to the poor radiometric performances which decrease the importance of the information derived from the observations and to the lack of a thermal channel that leads to an unreliable cloud mask.

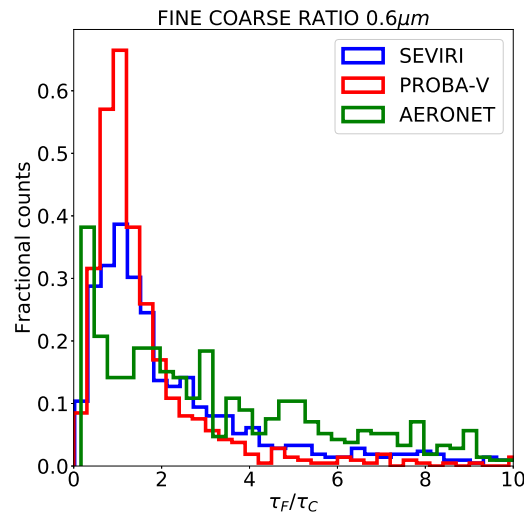


Fig. 15: Fine-coarse mode ratio distribution at $0.6 \mu\text{m}$ for from AERONET (redgreen) , and from CISAR applied to SEVIRI (blue) and PROBA-V (greenred) observations.

The CISAR potential to discriminate between the fine and coarse mode is analysed next. Figure 15 shows the fine and coarse mode ratio distribution related to AERONET (in red data (in green) and CISAR retrieval for SEVIRI (in blue) and PROBA-V (in greenred). It can be seen that the distribution related to CISAR retrievals from SEVIRI observations is in good agreement with the one associated to AERONET observations, whereas the retrieval from and PROBA-V observations seems seem to underestimate the fine mode concentration for $\tau_F/\tau_C > 2\tau_F/\tau_C > 3$. The percentage of cases where CISAR succeeds in retrieving a predominant fine mode contribution to the total AOT τ , ($\tau_F/\tau_C > 1$), is in fact equal to 81 equal to 80% when the retrieval is performed on SEVIRI acquisition and 6862% when CISAR is applied on to PROBA-V data. The latter This represents an improvement with respect to the Land Daily Aerosol (LDA) algorithm (Wagner et al. (2010), Table 4) where particles retrieved by AERONET as spherical were correctly characterise characterised by the algorithm only in the 12% of cases. This represents a decisive advantage of the proposed approach with a continuous variations of the aerosol properties in the solution space, as opposed to the use of a limited number of aerosol classes as in Wagner et al. (2010). The coarse particle characterisation retrieval appears to be more challenging for both satellite satellites. The percentage of cases where the coarse mode is correctly retrieved as predominant is 43% and 2730% for the retrieval from SEVIRI and PROBA-V observations respectively. The less accurate retrieval of the coarse mode compared to the fine mode is expected, as the considered wavelengths are less sensitive to the radii in the range of the coarse particles than to those of fine ones (Torres et al., 2017). A similar behaviour is also This can also be observed in Table 9 where the median magnitude of the coarse mode Jacobian is more than twice smaller than less than an half of the fine mode Jacobian.

6.3 Single scattering albedo and asymmetry factor

In Section Sect. 3.2 the solution space defined by the aerosol classes vertices has been described. CISAR retrieves the averaged SSA and asymmetry factor within this solution space from Eq. 8 and 9 of Part I, as linear combination of the micro-physical as linear combinations of the single scattering properties of each selected aerosol vertex. Figure (Eq. 8 and 9 of Part I). Figures 16 and 17 show the SSA and asymmetry factor distribution distributions related to the AERONET data and CISAR retrieval from both SEVIRI and PROBA-V observations. inversion product and CISAR retrievals. All the AERONET inversions are considered, without applying the quality test as in Holben et al. (2006). The three datasets show similar distributions, although spikes can be observed at the extremes of the CISAR retrievals distributions. These spikes correspond to the sides of the triangle delineated by the three selected vertices shown in Fig. 4: when the actual When the AERONET solution is located outside the solution space, CISAR cannot reach converge to it and the retrievals falls on the solution space boundaries, hence causing the spikes. The aerosol vertices selection as in Fig. 4, made to encompass about the 90% of the solutions as retrieved from AERONET inversion product, is conceived to limit the number of occurrences of these spikes. In

670 ~~Fig. 17 it can be noticed~~ Figure 17 shows that the g parameter distributions obtained from CISAR
~~applied to~~ PROBA-V observations is much narrower than the same distribution related to AERONET
and CISAR applied to SEVIRI retrievals observations. This is in line with what has been seen in
~~Section discussed in Sect. 6.2~~ on the poorer CISAR ~~performance~~ performances in retrieving the
predominant mode when applied to PROBA-V observations rather than the SEVIRI ones. In fact, as
675 in computing g the aerosol size distribution is the most important parameter to measure (Andrews
et al., 2006), an inexact estimation estimate of the dominant mode (fine or coarse mode) leads to an
erroneous measurement of the asymmetry parameter.

6.4 ~~Surface bihemispherical reflectance~~

~~CISAR retrieved BHR (blue dots) from SEVIRI (upper panel) and PROBA-V (lower panel) and~~
680 ~~MODIS Land Product (yellow triangle) averaged on SEVIRI and PROBA-V pixels over Zinder~~
~~Airport (Niger, Africa). The results are shown for the sensors band centred at $0.6 \mu\text{m}$ over 2015.~~
~~The vertical bars represent the CISAR retrieval uncertainty.~~

~~CISAR retrieved BHR from actual observations comparison with MODIS in all the processed~~
~~bands: $0.6 \mu\text{m}$ $0.8 \mu\text{m}$ $1.6 \mu\text{m}$ $0.6 \mu\text{m}$ $0.4 \mu\text{m}$ $0.8 \mu\text{m}$ $1.6 \mu\text{m}$ Number of points Correlation 0.925~~
685 ~~0.820 0.860 0.763 0.891 0.774 0.890 Root Mean Square Error 0.045 0.067 0.080 0.030 0.051 0.092~~
 ~~0.085 Mean Absolute Bias 0.038 0.053 0.067 0.026 0.042 0.064 0.068~~

~~CISAR BHR, computed from the RPV parameters, is compared with MODIS Land product~~
~~(Schaaf and Wang, 2015). To account for the different spatial sampling, the MODIS data have been~~
~~averaged on 5×5 km and 3×3 km for the comparison with the retrievals from SEVIRI and PROBA-V~~

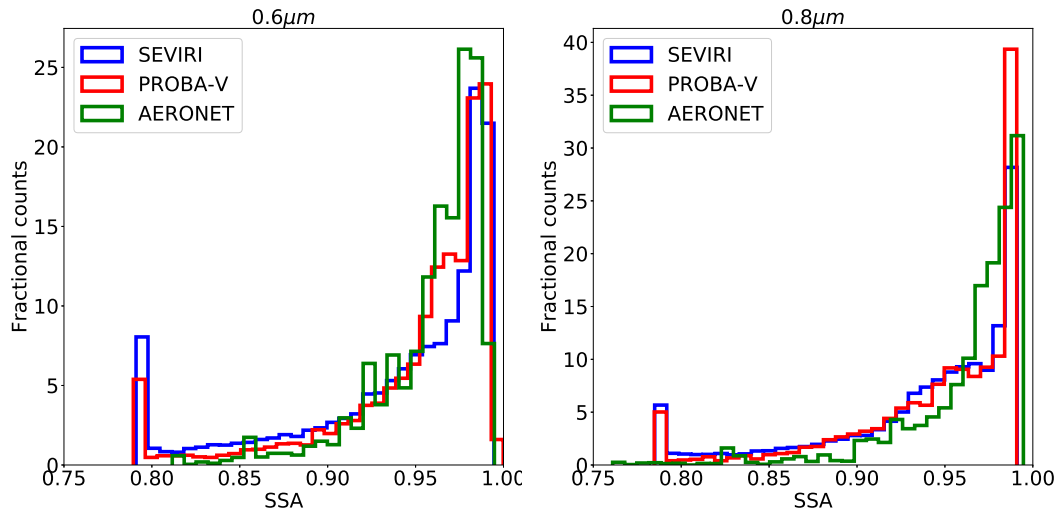


Fig. 16: SSA distributions at $0.6 \mu\text{m}$ (left panel) and $0.8 \mu\text{m}$ (right panel) for AERONET (~~red~~green),
CISAR applied to SEVIRI (blue) and to PROBA-V (~~green~~red).

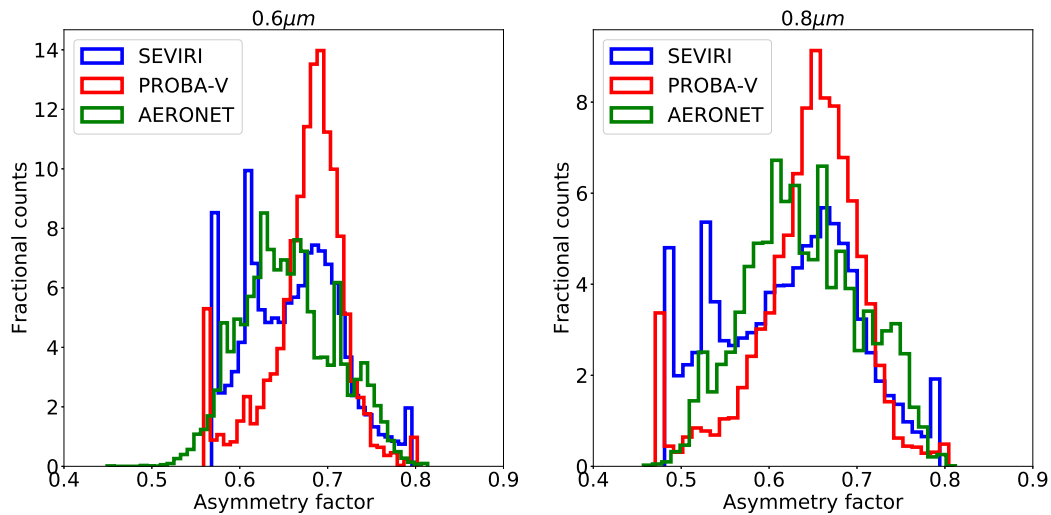


Fig. 17: Same as Figure 16 but for the asymmetry factor.

690 respectively. The results of this comparison are shown in Table 10 in terms of correlation, RMSE, and MAE. CISAR results show a high correlation with the MODIS product, higher than 0.800 in all the processed spectral bands, except the PROBA-V NIR band, which shows a correlation equal to 0.774. The density plots of CISAR BHR retrieval against MODIS data are included in the Supplement for all processed bands, for both satellites. Despite the instruments differences discussed in Section 2.5, CISAR retrievals and the MODIS Land Product dataset show similar seasonal trends. 695 Figure 13 shows the BHR timeseries over Zinder Airport (Niger, Africa), as retrieved from the CISAR algorithm applied to SEVIRI and PROBA-V observations and from MODIS Land Product. The rainy season, going from May 20 to October 5 (Weatherspark.com, 2018), is distinguishable in all the datasets, although CISAR retrieves a larger seasonal variation with respect to MODIS product. 700 The effect of the updating mechanism on the surface prior described in Section 2.4 is also visible, especially in Fig. 13b, where the retrieval uncertainty decreases in time, as the prior information on the surface is better defined.

7 Discussion and conclusion

This paper describes and evaluates the ~~CISAR algorithm when applied~~ [application of the CISAR algorithm](#) to satellite observations acquired from geostationary and polar orbiting instruments. The 705 theoretical aspects of CISAR, a new generic algorithm for the joint retrieval of surface reflectance and aerosol properties, with continuous variation of all the state variables in the solution space, are described in Part I. In the latter CISAR is applied to simulated noise free observations in the principal plane. This paper provides an evaluation of the algorithm in non ideal situations, *i.e.*, ~~when applied~~

710 ~~to~~ actual satellite observations acquired from both geostationary and polar orbiting satellites, namely SEVIRI and PROBA-V.

The proposed retrieval method relies on an OE approach which consists ~~in~~ of the inversion of ~~FASTRE~~ FASTRE, a simple radiative transfer model composed of two horizontal layers. The ~~first step of CISAR algorithm evaluation consists thus in the evaluation of the inverted forward model~~ (Section 2.5). ~~The FASTRE model is accurate within 1% to~~ evaluated in Sect. 2.5 showing an accuracy within 3% percent when compared to a complex 1D radiative transfer model. Higher uncertainties are observed in spectral bands affected by water vapour as a result of the limited vertical discretisation. ~~The FASTRE model capabilities to simulate actual observations has also been evaluated but revealed relative bias larger than 5%. This poor performance partially results from the~~ lack of accurate description of the state variables at the moment of the satellite overpasses.

The analysis of the information content of the satellite observations is performed in ~~Section 4~~. ~~Despite Sect. 4. Though~~ the PROBA-V instrument has one blue channel which is not present ~~on~~ in SEVIRI, the ~~frequent revisit rate of the latter provides better radiometric performances of the geostationary satellite provide~~ more information for the retrieval of surface reflectance and aerosol ~~properties than the former polar orbiting instrument.~~

The CISAR retrieval is ~~finally~~ evaluated against independent datasets. The retrieved AOT is compared ~~against to~~ AERONET data. A specific QI has been developed to disregard suspicious ~~retrieval and has been applied in this analysis~~ retrievals. With a RMSE of ~~0.173~~ 0.162 for SEVIRI and ~~0.214~~ 0.176 for PROBA-V, CISAR shows better performances when applied ~~on geostationary data, as expected from the analysis in Section 4 to the geostationary satellite.~~ CISAR retrieves the ~~micro-physical single scattering~~ aerosol properties assuming a linear behaviour of g and ω_0 in the solution space ~~in Fig. 4~~; although this assumption is not exactly true when far from pure single mode situations, CISAR retrieved aerosol properties distributions are in good agreement with the AERONET inversion products, especially when the algorithm is applied ~~on geostationary observation to geostationary observations~~, as discussed in ~~Section Sect.~~ 6.3. These differences are explained by the different information content associated to the ~~satellite observations acquired with different orbits~~ observations acquired by the two satellites. For both satellites, CISAR discrimination between fine and coarse mode is improved with respect to the LDA algorithm (Wagner et al., 2010), as the continuous variation of the aerosol properties in the solution space allows ~~a more accurate retrieval of the micro-physical~~ more accurate retrievals of the single scattering properties with respect to LUT-based approaches. The CISAR surface albedo is compared with ~~the~~ the MODIS product, showing a correlation higher than ~~0.77~~ 0.74 in all processed bands ~~-(to the exception of the NIR PROBA-V band)~~. ~~The better performances of CISAR in retrieving the surface reflectance rather than the AOT are explained by the larger contribution to the TOA BRF at the satellite of the surface. The little variance of the surface reflectance on a short time scale allows a good prior definition based on the previous CISAR retrievals.~~

Several aspects of the new CISAR algorithm would still require additional efforts to improve its performance. The ~~capability of the FASTRE model to provide an unbiased estimation of observed TOA BRF still remains to be clearly demonstrated. Cloud effects~~ cloud mask omission errors impact on the AOT overestimation at low optical thickness would also deserve additional work. The analysis of the Jacobian median values has revealed the very small magnitude of the fine and coarse mode AOT. ~~Spectral~~ Jacobians. The spectral and temporal constraints of the AOT variability play therefore a critical role in supporting the assessment of aerosol properties. However, these constraints might lead to an underestimation of ~~AOT retrieval at~~ the AOT for large values.

As pointed out in Part I, the limited number of state variables retrieved by CISAR allows the same algorithm to be applied ~~on~~ to sensors which have not been originally designed for aerosol or surface albedo retrieval. The possibility to apply the same algorithm ~~on~~ to data acquired by different ~~sensors~~ instruments for the retrieval of several ECVs presents a decisive advantage. ~~It as it~~ provides radiatively consistent ECVs ~~between themselves~~ derived from different sensors. Conversely, the use of separate methods for the retrieval of different variables might lead to a radiance bias, which has to be corrected preliminary to the assimilation of these variables (Thépaut, 2003). The effort for the assimilation of surface and atmospheric products could be reduced if the different ECVs are consistently derived with one single algorithm. The consistent retrieval of the state variables and the algorithm applicability to different sensors represent an important advantage for the Numerical Weather Prediction (NWP) community, whose main future challenges are related to a more consistent retrieval of Earth's system components and to the availability of more satellite data. ~~The latter makes desirable an algorithm applicable to different types of orbits and bands in order to have continuity in the dataset.~~

8 Supplement

~~Includes the scatterplots between~~ Included are the scatterplots of the BHR retrieved by CISAR ~~and the one delivered in the MODIS product versus the BHR delivered by MODIS~~ (Fig. S1, S2) ~~and~~, and a few examples of ~~CISAR high-AOT retrievals in comparison the CISAR high-AOT retrievals compared~~ with AERONET data.

9 Acknowledgements

Acknowledgements. This work has been performed in the framework of ESA projects aerosol_cci2 and PV-LAC under the contract 4000109874/14/I-NB and 4000114981/15/I-LG respectively. The authors would like to thank the reviewers for their fruitful suggestions.

References

- Andrews, E., Sheridan, P. J., Fiebig, M., McComiskey, A., Ogren, J. A., Arnott, P., Covert, D., Elleman,
780 R., Gasparini, R., Collins, D., Jonsson, H., Schmid, B., and Wang, J.: Comparison of methods for deriving
aerosol asymmetry parameter, *Journal of Geophysical Research*, 111, doi:doi:10.1029/2004JD005734, 2006.
- Chand, D., Wood, R., Ghan, S. J., Wang, M., Ovchinnikov, M., Rasch, J. P., Miller, S., Schichtel, B., and Moore,
T.: Aerosol optical depth increase in partly cloudy conditions, *Journal of Geophysical Research*, 117, 2012.
- DAAC, O.: MODIS Collection 5 Land Products Global Subsetting and Visualization Tool., 2017.
- 785 DAAC, O.: Terra and Aqua Moderate Resolution Imaging Spectroradiometer, <https://ladsweb.modaps.eosdis.nasa.gov/missions-and-measurements/modis/>, online, accessed 19 June 2018, 2018.
- Dee, D. P., Uppala, S. M., Simmons, A. J., Berrisford, P., Poli, P., Kobayashi, S., Andrae, U., Balmaseda, M. A.,
Balsamo, G., Bauer, P., Bechtold, P., Beljaars, A. C. M., van de Berg, L., Bidlot, J., Bormann, N., Delsol, C.,
Dragani, R., Fuentes, M., Geer, A. J., Haimberger, L., Healy, S. B., Hersbach, H., Hólm, E. V., Isaksen, L.,
790 Kållberg, P., Köhler, M., Matricardi, M., McNally, A. P., Monge-Sanz, B. M., Morcrette, J., Park, B., Peubey,
C., de Rosnay, P., Tavolato, C., Thépaut, J., and Vitart, F.: The ERA-Interim reanalysis: configuration and
performance of the data assimilation system, *Quarterly Journal of the Royal Meteorological Society*, 137,
553–597, doi:10.1002/qj.828, <https://rmets.onlinelibrary.wiley.com/doi/abs/10.1002/qj.828>, 2011.
- Dubovik, O., Sinyuk, A., Lapyonok, T., Holben, B. N., Mishchenko, M., Yang, P., Eck, T. F., Volten, H., Munoz,
795 O., Veihelmann, B., van der Zande, W. J., Leon, J. F., Sorokin, M., and Slutsker, I.: Application of spheroid
models to account for aerosol particle nonsphericity in remote sensing of desert dust, *Journal of Geophysical
Research-Atmospheres*, 111, 11 208–11 208, 2006.
- Dubovik, O., Herman, M., Holdak, A., Lapyonok, T., Tanré, D., Deuzé, J. L., Ducos, F., Sinyuk, A., and
Lopatin, A.: Statistically optimized inversion algorithm for enhanced retrieval of aerosol properties from
800 spectral multi-angle polarimetric satellite observations, *Atmospheric Measurement Techniques*, 4, 975–1018,
2011.
- Giles, D. N., Holben, B. N., Eck, T. F., Smirnov, A., Sinyuk, A., Schafer, J., Sorokin, M. G., and Slutsker, I.:
Aerosol Robotic Network (AERONET) Version 3 Aerosol Optical Depth and Inversion Products, American
Geophysical Union, Fall Meeting 2017, abstract #A110-01, 2017.
- 805 Govaerts, Y. and Lattanzio, A.: Retrieval Error Estimation of Surface Albedo Derived from Geostationary Large
Band Satellite Observations: Application to Meteosat-2 and -7 Data, *Journal of Geophysical Research*, 112,
doi:10.1029/2006JD007313, 2007.
- Govaerts, Y. and Luffarelli, M.: Joint Retrieval of Surface Reflectance and Aerosol Properties with Continuous
Variations of the State Variables in the Solution Space: Part I: Theoretical Concept, *Atmos. Meas. Tech.*
810 Discuss, pp. 1–27, doi:doi:10.5194/amt-2017-29, 2017.
- Govaerts, Y., Wagner, S., Lattanzio, A., and Watts, P.: Optimal estimation applied to the joint retrieval of aerosol
optical depth and surface BRDF using MSG/SEVIRI observations, chap. 11, Springer, 2008.
- Govaerts, Y., Sterckx, S., and Adriaensen, S.: Use of simulated reflectances over bright desert target as an
absolute calibration reference, *Remote Sensing Letters*, 4, 523–531, 2013.
- 815 Govaerts, Y., Luffarelli, M., and E., P.: CISAR-ATBD-V2.0, https://earth.esa.int/documents/700255/2632405/PV-LAC_ATMO_ATBD_IODD_V2.pdf/4408fa65-e644-4b2f-a8a7-e97b7e6f0de2, 2017.
- Govaerts, Y. M., Wagner, S., Lattanzio, A., and Watts, P.: Joint retrieval of surface reflectance and aerosol

- optical depth from MSG/SEVIRI observations with an optimal estimation approach: 1. Theory, *Journal of Geophysical Research*, 115, doi:10.1029/2009JD011779, 2010.
- 820 Hadamard, J.: Sur les problèmes aux dérivées partielles et leur signification physique., *Princeton University Bulletin*, pp. 49–52, 1902.
- Henderson, B. and Chylek, P.: The effect of spatial resolution on satellite aerosol optical depth retrieval, *IEEE Transactions on Geoscience and Remote Sensing*, 43, 1984 – 1990, doi:10.1109/TGRS.2005.852078, <https://ieeexplore.ieee.org/document/1499014>, 2005.
- 825 Holben, B. N., Eck, T. F., Slutsker, I., Smirnov, A., Sinyuk, A., Schafer, J., Giles, D., and Dubovik, O.: Aeronet’s Version 2.0 quality assurance criteria, *Proc.SPIE*, 6408, 6408 – 6408 – 14, doi:10.1117/12.706524, <https://doi.org/10.1117/12.706524>, 2006.
- Hsu, N. C., Jeong, M., Bettenhausen, C., Sayer, A., Hansell, R., Seftor, C., Huang, J., and Tsay, S.: Enhanced Deep Blue Aerosol Retrieval Algorithm: The Second Generation, *Journal of Geophysical Research: Atmospheres*, 118, 9296–9315, 2013.
- 830 Hubanks, P.: MODIS Atmosphere QA Plan for Collection 061, https://modis-atmos.gsfc.nasa.gov/sites/default/files/ModAtmo/QA_Plan_C61_Master_2017_03_15.pdf, 2017.
- Jiang, X., Liu, Y., Yu, B., and Jiang, M.: Comparison of MISR aerosol optical thickness with AERONET measurements in Beijing metropolitan area, *Remote Sensing of Environment*, 107, 45 – 53, doi:<https://doi.org/10.1016/j.rse.2006.06.022>, <http://www.sciencedirect.com/science/article/pii/S0034425706004329>, multi-angle Imaging SpectroRadiometer (MISR) Special Issue, 2007.
- 835 Kaufman, Y. J., Tanré, D., Gordon, H. R., Nakajima, T., Lonoble, J., Frouin, R., Grassl, H., Herman, M., King, M. D., and Teillet, P. M.: Passive remote sensing of tropospheric aerosol and atmospheric correction for the aerosol effect, *Journal of Geophysical Research: Atmospheres*, 102, 16 815–16 830, 1997.
- 840 Kinne, S., O’Donnel, D., Stier, P., Kloster, S., Zhang, K., Schmidt, H., Rast, S., Giorgetta, M., Eck, T. F., and Stevens, B.: MAC-v1: A New Global Aerosol Climatology for Climate Studies, *Journal of Advances in Modeling Earth Systems*, 5, doi:10.1002/jame.20035, 2013.
- Kokhanovsky, A. A., Breon, F. M., Cacciari, A., Carboni, E., Diner, D., Di Nicolantonio, W., Grainger, R. G., Grey, W. M. F., Höller, R., Lee, K. H., Li, Z., North, P. R. J., Sayer, A. M., Thomas, G. E., and von
- 845 Hoyningen-Huene, W.: Aerosol remote sensing over land: A comparison of satellite retrievals using different algorithms and instruments, *Atmospheric Research*, 85, 372–394, doi:doi:10.1016/j.atmosres.2007.02.008, 2007.
- Li, X. and Strahler, A. H.: Geometrical-optical bidirectional reflectance modeling of the discrete crown vegetation canopy: Effect of crown shape and mutual shadowing., *IEEE Transactions on Geoscience and Remote Sensing*, 30, 276–292, 1992.
- 850 Luffarelli, M., Govaerts, Y., and Damman, A.: Assessing hourly aerosol properties retrieval from MSG/SEVIRI observations in the framework of aerosol-cci2, in: *Living Planet Symposium 2016, Prague, Czech Republic, Prague, Czech Republic*, 2016.
- Maignan, F., Bréon, F. M., and Lacaze, R.: Bidirectional reflectance of Earth targets: Evaluation of analytical models using a large set of spaceborne measurements with emphasis on the Hot Spot, *Remote Sensing of Environment*, pp. 210–220, 2003.
- 855 Marquardt, D.: An Algorithm for Least-Squares Estimation of Nonlinear Parameters, *SIAM Journal on Applied*

Mathematics, 11, 431–441, 1963.

- 860 Mei, L., Rozanov, V., Vountas, M., Burrows, J., and Jafariserajehlou, S.: XBAER: A versatile algorithm for the retrieval of aerosol optical thickness from satellite observations, *Geophysical Research Abstracts*, 19, 2017.
- Meteo France: Algorithm Theoretical Basis Document for “Cloud Products” (CMa-PGE01 v3.2, CT-PGE02 v2.2 & CTTH-PGE03 v2.2), Tech. Rep. CTTH-PGE03 v2.2, 2013.
- 865 Pinty, B., Roveda, F., Verstraete, M. M., Gobron, N., Govaerts, Y., Martonchik, J. V., Diner, D. J., and Kahn, R. A.: Surface albedo retrieval from Meteosat: Part 1: Theory, *Journal of Geophysical Research*, 105, 18 099–18 112, 2000.
- Rahman, H., Pinty, B., and Verstraete, M. M.: Coupled surface-atmosphere reflectance (CSAR) model. 2. Semiempirical surface model usable with NOAA Advanced Very High Resolution Radiometer Data, *Journal of Geophysical Research*, 98, 20,791–20,801, 1993.
- 870 Rodgers, C. D.: Inverse methods for atmospheric sounding, Series on Atmospheric Oceanic and Planetary Physics, World Scientific, 2000.
- Ross, J. K.: The radiation regime and architecture of plant stands., The Hague, The Netherlands: Dr Junk W., doi:10.1007/978-94-009-8647-3, 1981.
- Schaaf, C. and Wang, Z.: MCD43A1 MODIS/Terra+Aqua BRDF/Albedo Model Parameters Daily L3 Global - 500m V006, doi:<https://doi.org/10.5067/MODIS/MCD43A1.006>, 2015.
- 875 Seidel, F. C., Kokhanovsky, A. A., and Schaepman, M. E.: Fast and simple model for atmospheric radiative transfer, *Atmospheric Measurement Techniques*, 3, 1129–1141, doi:10.5194/amt-3-1129-2010, <https://www.atmos-meas-tech.net/3/1129/2010/>, 2010.
- Sissenwine, N., Dubin, M., and S., T.: US Standard Atmosphere, 1976.
- 880 Sterckx, S., Livens, S., and Adriaensen, S.: Rayleigh, Deep Convective Clouds, and Cross-Sensor Desert Vicarious Calibration Validation for the PROBA-V Mission, *IEEE Transactions on Geoscience and Remote Sensing*, 51, 2013.
- Sterckx, S., Benhadj, I., Duhuoux, G., Livens, S., Dierckx, W., Goor, E., and Adriaensen, S.: The PROBA-V Mission: Image Processing and Calibration, *International Journal of Remote Sensing*, 35, 2565–88, doi: <https://doi.org/10.1080/01431161.2014.883094>, 2014.
- 885 Sun, L., Bilal, M., Tian, X., Jia, C., Guo, Y., and Mi, X.: Aerosol Optical Depth Retrieval over Bright Areas Using Landsat 8 OLI Images, Tech. rep., doi:10.3390/rs8010023, <http://www.mdpi.com/journal/remotesensing>, 2016.
- Thépaut, J.: Satellite Data Assimilation in Numerical Weather Prediction: an Overview, *Data Assimilation for the Earth System*, 26, doi:https://doi.org/10.1007/978-94-010-0029-1_19, 2003.
- 890 Torres, B., Dubovik, O., Fuertes, D., Schuster, G., Cachorro, V. E., Lapyonol, T., Goloub, P., Blarel, L., Barreto, A., Mallet, M., Toledano, C., and Tanré, D.: Advanced characterisation of aerosol size properties from measurements of spectral optical depth using the GRASP algorithm, *Atmospheric Measurement Techniques*, 10, 3743–3781, 2017.
- 895 Wagner, S. C., Govaerts, Y. M., and Lattanzio, A.: Joint retrieval of surface reflectance and aerosol optical depth from MSG/SEVIRI observations with an optimal estimation approach: 2. Implementation and evaluation, *Journal of Geophysical Research*, 115, doi:10.1029/2009JD011 780, 2010.
- Wang, Y.: Regularization for inverse models in remote sensing, *Progress in Physical Geography: Earth and En-*

vironment, 36, 38–59, doi:10.1177/0309133311420320, <https://doi.org/10.1177/0309133311420320>, 2012.

900 Wanner, W., Li, X., and Strahler, A. H.: On the derivation of kernels for kernel-driven models of bidirectional reflectance., *Journal of Geophysical Research*, 100, 21 077–21 089, 1995.

Weatherspark.com: Weatherspark.com, 2018, <https://weatherspark.com/y/148098/Average-Weather-at-Zinder-Airport-Niger-Year-Round>, online, accessed 30 May 2018, 2018.

Wolters, E., Dierckx, W., Iordache, M.-D., and Swinnen, E.: PROBA-V Products User Manual v3.01, 2018.